APPLICATIONS OF DUAL-SEED OPTICAL COMB SOURCES IN TELECOMMUNICATIONS AND SIGNAL PROCESSING

by

Hong-Fu Ting

A dissertation submitted to Johns Hopkins University in conformity with the requirements for the degree of Doctor of Philosophy

Baltimore, Maryland

January, 2017

Abstract

With the continuing demand for high-speed and efficient operation or transmission, photonic approaches to signal processing systems and communication networks become indispensable due to the high bandwidth capacities. Particularly, by utilizing various nonlinear optical effects, it is possible to achieve a wide variety of bandwidth-demanding applications with minimal system resources. A device based on nonlinear optical processes can simultaneously provide a multitude of channels, greatly removing the unnecessary parallel processing units and thus reducing the complexity of system designs. In this regard, dual-seed optical comb sources based on parametric mixing have been of great interest since this apparatus efficiently enhance the scalability of a system.

The dual-seed optical comb sources can be applied to diverse areas in telecommunications and signal processing. In this study, two primary target applications which involve the optical comb sources include wavelength multicasting and analog-to-digital conversion, respectively. Wavelength multicasting, an essential functionality in optical communication networks, can accomplish simultaneous delivery of a high-rate data stream from one single routing

node to a group of destinations at different assigned wavelengths. Moreover, the parallelism supported by wavelength multicasting greatly benefits various high-speed optical signal processing systems. The other application investigated here is the analog-to-digital conversion which becomes necessitated due to the rapid progress in digital signal processing technology. Notably, in comparison with conventional electronic counterparts, photonic analog-to-digital converters have the advantages of broad bandwidth, low timing jitter and high sampling rate.

The first part of this work is focused on the study of dual-seed optical comb sources. The bandwidth of the comb spectrum is increased by means of a longitudinally varying strain plan along the optical fiber. In the second part, a wavelength multicasting scheme based on the optical comb source is investigated. Importantly, the modulation format transparency provided by our proposed scheme is experimentally demonstrated. Lastly, a photonic approach to analog-to-digital conversion is achieved with the aid of a dual-seed optical comb source. The folding transfer functions for optical quantization are efficiently created due to the generation of phase harmonics through parametric processes associated with the optical comb source.

Primary Reader: Dr. Mark A. Foster

Secondary Reader: Dr. Jacob B. Khurgin

Acknowledgments

I would like to express my sincere gratitude to my research advisor Dr. Mark A. Foster for the continuous support and constructive advice on my study. His guidance and patience prompt me to go through the odyssey over the past years.

Besides my supervisor, I am deeply thankful to the rest of my dissertation committee members Dr. Jacob B. Khurgin and Dr. Amy C. Foster for their valuable and insightful comments on this work. In particular, Prof. Khurgin renders me not only the systematic knowledge of professional realm but also an opportunity to gain teaching experience, both of which are greatly useful for me. I am grateful to my Graduate Board Oral (GBO) committee members Dr. James B. Spicer, Dr. Theodore O. Poehler, and Dr. Nina Markovic for their helpful suggestions.

In addition, my appreciation also goes to my collaborators Dr. A. Brinton Cooper and Dr. Yi Yang, who give me an opportunity to be involved in my first research project. I appreciate the kindness and encouragement from Dr. Cooper.

I would like to extend my heartfelt thanks to the current and former members of the Ultrafast and Nonlinear Photonics Group: Dr. Keith G. Petrillo, Jasper Stroud, Milad Alemohammad, Bryan Bosworth, Jaewook Shin, Amit Bhatia, and Iskandar

Atahodjaev for their great assistance and generous sharing. I have much gratitude to the members of the Integrated Photonics Laboratory: Dr. Ke-Yao Wang, Hongcheng Sun, Kangmei Li, and Michael Kossey for their support and discussions.

I am sincerely indebted to my friends Dr. Guilin Liu, Dr. Ke Hu, and Shanshan Huang, who broaden my view of the world and stimulate my thoughts during my graduate study. Due to their diverse professional background, I am always able to learn something exciting.

My deepest gratitude goes to my beloved family for their absolute confidence in me. My parents always back me up all through these years, and my sister gives me unreserved support without a word of complaint. Last but not least, a special thanks goes to my wife for helping me walk through all the difficulties and being my strongest backing.

Contents

CONTENTS

List of Tables

List of Figures

LIST OF FIGURES

LIST OF FIGURES

Chapter 1

Introduction

This chapter is intended to provide an introductory overview that discusses the essentials of optical frequency combs and explains the cause of nonlinear optics. Section 1.1, serving as a prologue to the story, starts from the remarks on laser fundamentals. The progress in laser science and technology leads to the development of optical frequency combs and the completeness of study on nonlinear optics. Basic knowledge of optical frequency combs based on mode-locked lasers is presented in Section 1.2. This type of optical sources finds applications in various areas, particularly, in metrology and spectroscopy. In section 1.3, the origin of nonlinear optical phenomena is briefly explained by introducing the polarization density and the wave equation.

1.1 Introductory Remarks

In Chinese myths and legends, Suiren introduced the operation of drilling wood for fire. In Greek mythology, Prometheus stole fire from Olympus for humanity.

Irrespective of the authenticity of the myths and legends, the use of fire as a source of light and energy indeed promoted the progress of civilization. As fire is to ancient society, so is laser source to modern science and technology.

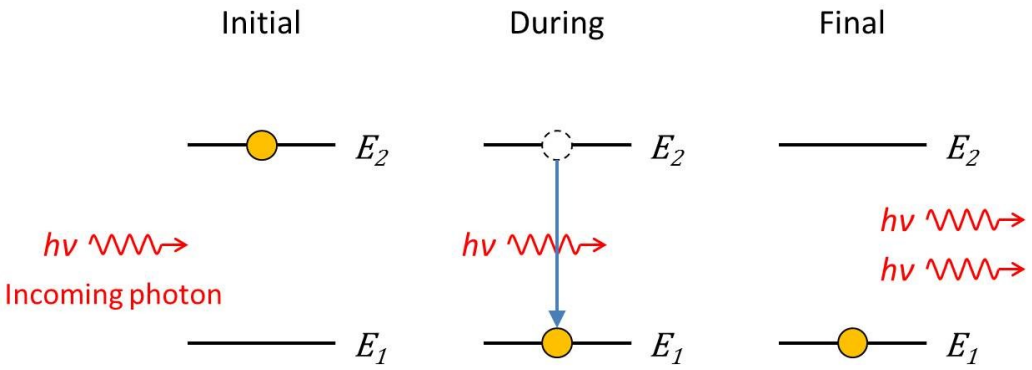

Fig. 1.1 The stimulated emission process. An incident photon of energy $h\nu = E_2 - E_1$ interact with an electron at an excited state E_2. The electron transit down to a lower energy state E_1, and a new photon identical to the original photon is produced.

The acronym LASER stands for Light Amplification by Stimulated Emission of Radiation. As indicated in the name of laser, stimulated emission is the foundation for achieving photon amplification. In the process of stimulated emission, an incoming photon of specific energy $h\nu = E_2 - E_1$ interacts with an excited electron and induces this electron at a higher energy level E_2 to transit down to a lower energy level E_1, as shown in Fig. 1.1. This downward transition produces a new photon, and the frequency, phase, direction, and polarization of the newly created photon are identical to those of the incident photon. In other words, one incoming photon results in two coherent photons with the same characteristics so that the light amplification can be achieved. A condition called population inversion is required In order to acquire the stimulated emission for laser operation,

representing a majority of electrons must be at the higher energy level. However, it is unable to obtain population inversion in practice by using a two-level system due to the equilibrium of upward excitation and downward emission in the steady state. Therefore, either a three-level or a four-level system is often used for laser operation.

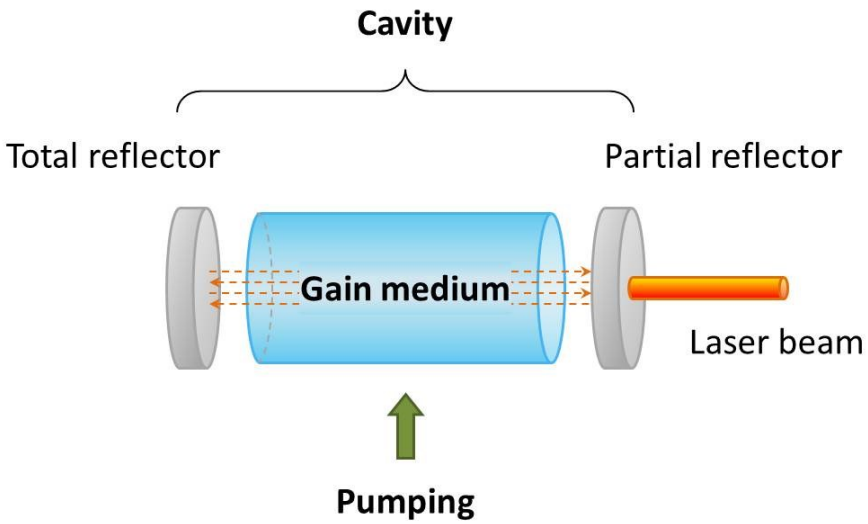

Fig. 1.2 Basic elements of laser. A laser system involves at least three basic elements including a gain medium, a pumping source, and an optical cavity.

From the aforementioned principle and requirement, as shown in Fig. 1.2, a laser system consists of at least three primary elements including a gain medium, a pumping mechanism, and an optical cavity. First, various materials can be utilized as the gain media, such as dye, gas, crystal, semiconductor, and rare-earth-doped fiber. The gain medium determines the range of operating wavelength provided by the laser. Second, an electrical or optical pumping can be used for injecting energy from external source into the gain medium and exciting the electrons at a lower energy

level to a higher energy level. Lastly, an optical cavity formed between two reflectors allows photons to reflect back and forth, and hence enhances the photon concentration (radiation intensity) through a series of stimulated emissions. From a wave point of view, light waves confined within an optical cavity reflect back and forth between two reflectors. Those traveling waves in opposite directions can interfere and give rise to a standing wave. To produce a standing wave, the cavity length is required to be a multiple of half-wavelengths. Consequently, only certain standing waves with a characteristic set of discrete wavelengths can survive in the optical cavity, and these probable standing waves are called cavity modes.

According to intensity characteristics of output light in time domain, lasers can be classified into two categories including continuous-wave (CW) lasers and pulsed lasers. With steady-state pumping, a CW laser outputs a constant light intensity over time. The other is the pulsed lasers which produce short pulses with high peak power. Pulse lasers can be achieved by using either Q-switching or mode-locking techniques. Typically, the pulse duration produced by a Q-switched laser is limited to the range of nanosecond due to a finite cavity lifetime [1]. On the other hand, mode-locked lasers can output ultrafast pulses with pulse duration on a picosecond or further down to femtosecond time scale.

The invention of lasers leads to the advancement of science and technology. Particularly, the breakthrough innovations in laser technology enable the emergence of optical frequency combs and various nonlinear optical effects. Therefore, the main topics covered in the rest of this chapter are optical frequency

combs based on mode-locked lasers and the origin of nonlinear optical phenomena, respectively.

1.2 Basics of Optical Frequency Combs

A series of discrete and equidistant spectral components in optical domain form an optical frequency comb which enables diverse applications in metrology [2], spectroscopy [3], astronomy [4], as well as communications and signal processing [5], as presented in Fig. 1.3. In these applications, a conventional type of optical frequency combs using mode-locked lasers (MLLs) plays an important role, and therefore it is suitable to start with the discussion on the MLL-based frequency combs [6-8].

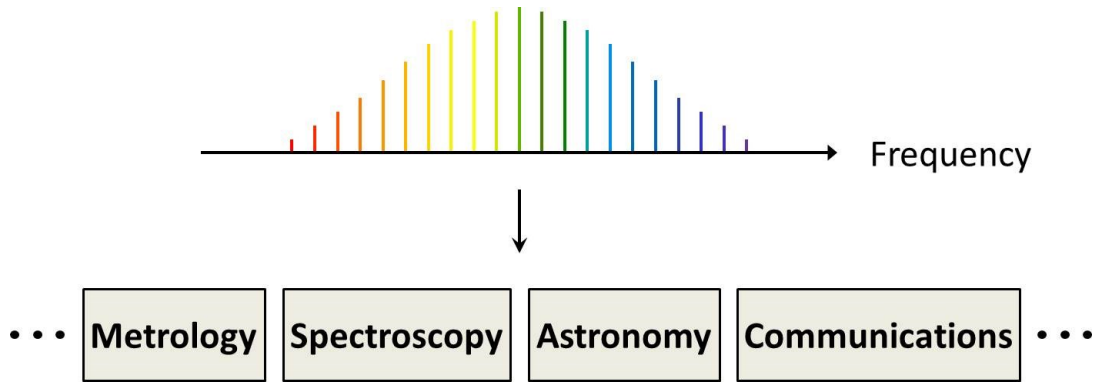

Fig. 1.3 A schematic diagram of an optical frequency comb spectrum. The spectrum consists of a multitude of equidistant comb components. Optical frequency combs can be applied to a wide variety of applications in metrology, spectroscopy, astronomy, and telecommunications and signal processing.

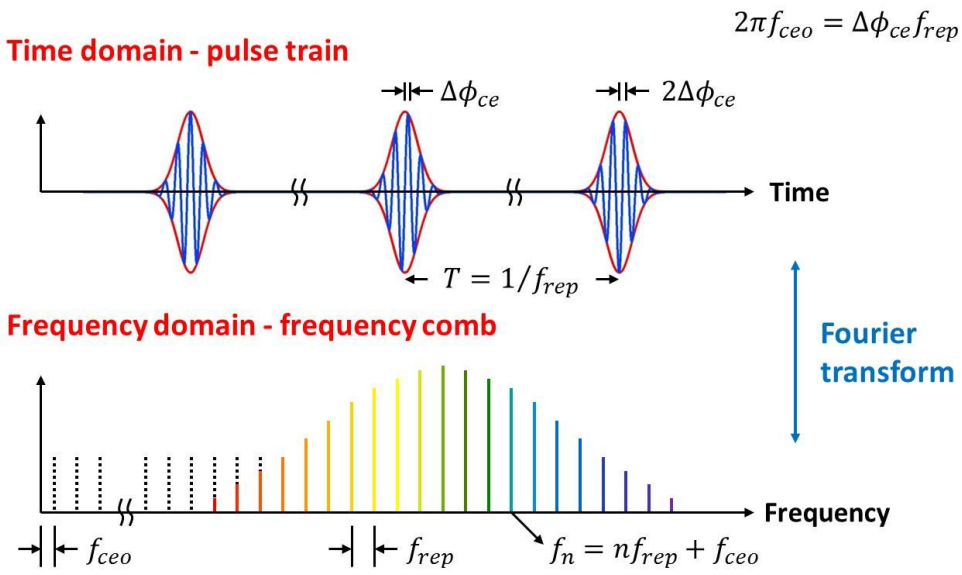

Fig. 1.4 Principle of an optical frequency comb based on mode-locked lasers. A mode-locked laser outputs a periodic train of ultrashort pulses in time domain, and a frequency comb is generated in frequency domain. The characteristics between two domains are linked by the Fourier transformation.

1.2.1 Principle of Operation

Mode-locked lasers directly promotes the generation of optical frequency combs. To understand the MLL-based frequency combs, the characteristics in the time and frequency domain have to be investigated, respectively, as shown in Fig. 1.4. In the time domain, mode-locked lasers produce a periodic train of ultrashort pulses by building a fixed phase relationship between all of the lasing cavity modes. The successive pulses are separated by the round-trip time T taken for a pulse to travel within the cavity. All of the pulses consist of the pulse envelope (red) traveling with the group velocity and the carrier wave (blue) propagating with the phase velocity. Due to the dispersion, i.e. the difference between group and phase velocities within

the cavity, the pulses are not exactly identical. The carrier wave shifts with respect to the peak of the pulse envelope by a phase change $\Delta\phi_{ce}$ after each round trip.

Fourier analysis is a powerful tool that links the time and frequency domain. In mathematics, the Fourier transform of an impulse train is still an impulse train. For a pulse train with a constant time interval T between successive pulses, the corresponding spectrum consists of a multitude of evenly spaced comb frequencies with comb spacing equal to the repetition rate f_{rep}. This repetition rate, f_{rep}, is inversely proportional to the time interval T. In addition to the repetition rate, the other characteristic quantity in the frequency domain is the carrier-envelope offset frequency, f_{ceo}, due to the aforementioned dispersion within the cavity. As a result, this also means that the comb lines are not exactly at the integer multiples of the repetition frequency if both of the repetition frequency and the carrier-envelope offset frequency are taken into account.

It is evidently validated with Fourier analysis that a time shift results in a linear phase shift with frequency. Therefore, for a time shift of T which is now the time interval between consecutive pulses, the corresponding phase is ωT at an angular frequency ω. If we further consider the contribution to phase from the pulse-to-pulse carrier-envelope phase shift $\Delta\phi_{ce}$, then the total phase change between consecutive pulses becomes $\omega T - \Delta\phi_{ce}$ at the angular frequency ω. This total phase change is required to be $2n\pi$ for constructive interference, and hence the frequency of the nth comb line can be expressed as

$$f_n = nf_{rep} + f_{ceo} \tag{1.1}$$

with $2\pi f_{ceo} = \Delta\phi_{ce} f_{rep}$. Thus, the comb offset from exact harmonics of the repetition frequency corresponds to the pulse-to-pulse carrier-envelope phase shift.

1.2.2 Self-referencing Technique

The above equation connects an optical frequency of a comb line and two radio frequencies including the repetition frequency and the carrier-envelope offset frequency. In order to find the optical frequencies (or absolute frequencies) of comb components, both of the repetition rate and the offset frequency are indispensable. Here, the mode index of a comb line, n, is a large integer of order 10^5 to 10^6, and the repetition frequency typically ranges from a hundred of megahertz to a few gigahertz depending on the cavity length. The last key to the absolute frequency of the frequency comb is to determine the carrier-envelope offset frequency.

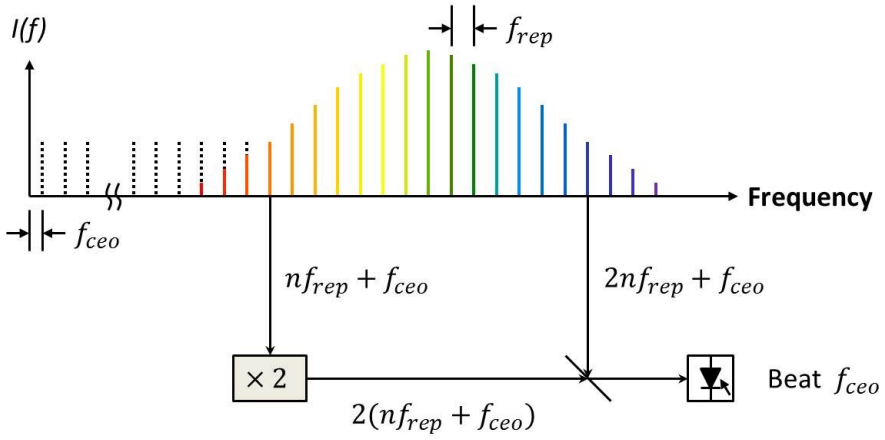

Fig. 1.5 A self-referencing technique. The beat note between two optical frequencies at $2f_n$ and f_{2n} can be measured to obtain the offset frequency and thus characterize the absolute frequency of comb components.

As seen in Fig. 1.5, a self-referencing technique [9] is introduced to precisely measure the comb offset and hence to fully characterize the absolute frequency of the comb lines. In an octave comb spectrum which spans a factor of two in frequency, both of a comb component with index n at the red side (f_n) and its corresponding component with index $2n$ at the blue side (f_{2n}) are simultaneously present. Meanwhile, the comb component with index n is frequency doubled by utilizing a second harmonic crystal so that a new frequency at $2f_n$ can be generated. Finally, measuring the beat note between the modes at f_{2n} and $2f_n$ can obtain the carrier-envelope offset frequency, f_{ceo}.

$$2f_n - f_{2n} = \left(2nf_{rep} + 2f_{ceo}\right) - \left(2nf_{rep} + f_{ceo}\right) = f_{ceo} \tag{1.2}$$

Once both of the repetition frequency and the offset frequency are known, the absolute frequency of the comb components can be determined.

1.3 Origin of Nonlinear Optics

In addition to optical frequency combs discussed in the previous section, various nonlinear optical phenomena have successively been discovered and studied after the emergence of lasers. The first demonstration of second-harmonic generation by Franken and coworkers in 1961 [10], which used a ruby laser realized in 1960, is generally regarded as the beginning of the study of nonlinear optics [11]. Later, until optical fibers were produced and further improved to reduce propagation losses, it became possible to use optical fibers as nonlinear media.

It is important to note that nonlinear optical effects arise due to the interaction between intense light and the medium in which the light propagates, rather than the strong lightwave itself [12]. This indicates at least two characteristics of nonlinear optical behavior. First, in addition to the need for intense light, the properties of materials play an important role in the generation of nonlinear optical effects. Second, we can use light to control or manipulate light through nonlinear medium since the modification of the properties of materials by an optical field can further alter another optical field. Before utilizing suitable nonlinear effects to achieve desired functionalities in diverse applications, we have to search for the cause of formation of nonlinear optics. In this section, the origin of nonlinear optics (or nonlinear fiber optics) will be briefly discussed by examining the polarization density and the wave equation in nonlinear media.

1.3.1 Polarization Density in Nonlinear Media

Dielectric materials contain bound charges, i.e. electrons in dielectric media are attached to atoms or molecules. In spite of the macroscopic neutrality of molecules in dielectrics, the presence of an external electric field forces positive and negative charges to displace in opposite directions. The tiny displacements of opposite charges create electric dipoles described by dipole moments. Some molecules, called polar molecules, have permanent dipole moments [13]. As depicted in the left of Fig. 1.6, when an external electric field is absent, the electric dipoles possess random orientations and thus no net dipole moment is established macroscopically. On the

other hand, the right of Fig. 1.6 shows the situation under the presence of an external electric field. If an external field is applied to the dielectric, individual dipoles rotate due to torque and tend to align with the applied electric field, which leads the medium to become polarized. Therefore, a net dipole moment is created in a polarized medium, and the polarization density used to characterize the material is defined as net dipole moment per unit volume.

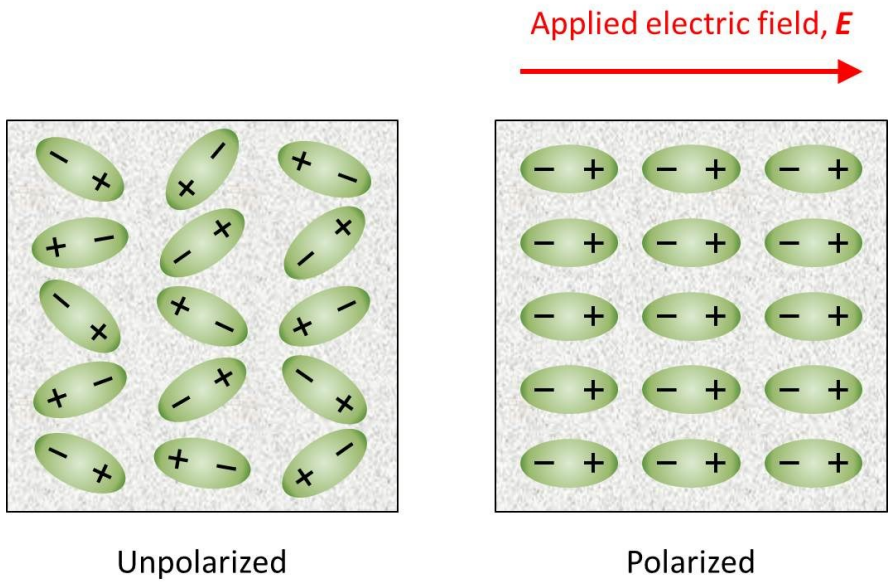

Fig. 1.6 Polarization of a dielectric medium. Left: electric dipoles are randomly distributed over an unpolarized medium when an external electric field is absent. Right: when an external electric field is present, electric dipoles are aligned with the applied field, and this medium is said to be polarized.

In other words, a dielectric material responds to an applied electric field E by establishing a polarization density P, and the properties of the material are described by the relation between the electric field E and the polarization density P. Note that, for simplicity, these two quantities are expressed in terms of scalar form.

In a linear medium, the polarization density is proportional to the electric field, and the two quantities are linked by the linear relation

$$P = \varepsilon_0 \chi^{(1)} E \tag{1.3}$$

where ε_0 is the permittivity of free space and $\chi^{(1)}$ is the first-order susceptibility or linear susceptibility. This linear behavior can be interpreted as the case of harmonic oscillator in Lorentz model. In this classical model of harmonic oscillator, we consider the Coulomb force between the nucleus and the electron as the restoring force of a spring. The linear relation between the polarization density and the electric field is analogous to that between the restoring force and the displacement described in the Hooke's law [12].

The medium response to light becomes nonlinear for intense optical fields which can be provided by laser sources. It means a nonlinear medium is described by a nonlinear relation between the polarization density and the electric field

$$P = \varepsilon_0 \chi^{(1)} E + \varepsilon_0 \chi^{(2)} E^2 + \varepsilon_0 \chi^{(3)} E^3 + \cdots \tag{1.4}$$

where the coefficients $\chi^{(2)}$ and $\chi^{(3)}$ are the second-order and third-order susceptibilities, respectively. The higher terms not shown in the expression are negligible due to the rapid decrease of higher-order susceptibilities. While the first term with the linear susceptibility dominates the total induced polarization density, the significance of the nonlinear terms arises when the optical field becomes comparable to the interatomic electric fields which typically range from 10^8 to 10^{10} V/m [14]. The third-order susceptibility $\chi^{(3)}$ is present in all dielectrics, and the

second-order susceptibility $\chi^{(2)}$ exists only in certain crystals without inversion symmetry. For optical fibers made of silica glasses, $\chi^{(2)}$ vanishes since a SiO_2 molecule possesses a center of symmetry [15,16]. Therefore, the third-order susceptibility $\chi^{(3)}$ accounts for lowest-order nonlinear effects which occur in optical fiber.

Generally, for resonant effects, a quantum mechanical approach is required to give a proper explanation for the nonlinear susceptibilities which arise from bound electrons. However, as an auxiliary tool for analyzing non-resonant effects, we still can consider the classical Lorentz model in which an anharmonic oscillation of a bound electron is driven by a strong field [11,17]. In this situation, the extension or compression of the analogous spring is large, and thus the relation between the restoring force and the displacement of the electron now becomes nonlinear.

1.3.2 Wave Equation for Nonlinear Media

Maxwell's equations govern the propagation of electromagnetic waves. Hereinafter, these equations are given in MKS units and all vector quantities are denoted by boldface symbols

$$\nabla \cdot \boldsymbol{D} = \rho_f \tag{1.5}$$

$$\nabla \cdot \boldsymbol{B} = 0 \tag{1.6}$$

$$\nabla \times \boldsymbol{E} = -\frac{\partial \boldsymbol{B}}{\partial t} \tag{1.7}$$

$$\nabla \times \boldsymbol{H} = \boldsymbol{J} + \frac{\partial \boldsymbol{D}}{\partial t} \tag{1.8}$$

where $\boldsymbol{E}$ and $\boldsymbol{H}$ represent the electric and magnetic fields, respectively, and the corresponding electric and magnetic flux densities, $\boldsymbol{D}$ and $\boldsymbol{B}$, describe the influence of the fields on the matter. The charge density ρ_f and the current density $\boldsymbol{J}$ are extraneous sources for the electric and magnetic fields. In a medium, the flux densities $\boldsymbol{D}$ and $\boldsymbol{B}$ are bridged to the fields $\boldsymbol{E}$ and $\boldsymbol{H}$ through the following constitutive relations

$$\boldsymbol{D} = \varepsilon_0 \boldsymbol{E} + \boldsymbol{P} \tag{1.9}$$

$$\boldsymbol{B} = \mu_0 (\boldsymbol{H} + \boldsymbol{M}) \tag{1.10}$$

where the universal constants ε_0 and μ_0 are the permittivity and permeability of free space, and $\boldsymbol{P}$ and $\boldsymbol{M}$ are the induced polarization density and magnetization density, respectively.

Here, we now can consider a practical case in optical fibers. Optical fibers are basically made of silica glasses, which are nonmagnetic ($\boldsymbol{M}$ = 0). The charge density ρ_f = 0 and the current density $\boldsymbol{J}$ = 0 due to the absence of free charges in optical fibers. From Eqs. (1.4) and (1.9), it evidently reveals that the nonlinearity which resides in the polarization density enters into the Maxwell's equations (and the wave equation shown later) through the constitutive relation. Therefore, the nonlinear response (nonlinear terms in Eq. (1.4)) to the electric field can couple back into the field, leading to the generation of nonlinear optical effects.

With the aid of the constitutive relations, using the Maxwell's equations yields the wave equation [11,12] that governs the propagation of light waves in a nonlinear medium

$$\nabla^2 \boldsymbol{E} - \frac{n^2}{c^2}\frac{\partial^2 \boldsymbol{E}}{\partial t^2} = \mu_0 \frac{\partial^2 \boldsymbol{P_{NL}}}{\partial t^2} \tag{1.11}$$

where n is the linear index of refraction due to the linear term in the total induced polarization density, and c is the speed of light in vacuum. The nonlinear part of the polarization density, $\boldsymbol{P_{NL}}$, is called the nonlinear polarization. This nonlinear medium response can be regarded as a driving source in the above inhomogeneous equation. The nonlinear wave equation also indicates the origin of nonlinear optical effects and lays the foundation for the theory of nonlinear optics.

Chapter 2

Dual-seed Optical Comb Sources

In the previous chapter, an important but not the only type of optical frequency combs which exploits mode-locked lasers (MLLs) is discussed. With the increasing demand and the rapid growth of technology, other novel solutions to realization of optical frequency combs have been continually proposed. In this chapter, to begin with, a classification of optical frequency comb sources is given here. Currently, four types of optical frequency combs based on various mechanisms and devices are often used in numerous applications. They are (1) MLL-based, (2) modulator-based [18,19], (3) microresonator-based [20-23], and (4) dual-seed optical frequency combs. This chapter is mainly focused on the dual-seed optical comb sources which enable the functionalities of wavelength multicasting and photonic analog-to-digital conversion (see Chapter 3 and Chapter 4).

2.1 Fundamental Mechanisms

This section is designed for introducing the basic mechanisms closely related to the generation of dual-seed optical comb sources. These important mechanisms include group velocity dispersion (GVD), compression of chirped pulses, and four-wave mixing (FWM). First, GVD results in pulse broadening when pulses propagate along an optical fiber, and fiber dispersion is crucial for both linear and nonlinear regimes. Next, compression of chirped pulses can increase peak power of the pulses, and thus the compressed pulses with enhanced peak power are allowed to experience a large nonlinear phase shift in the following nonlinear medium. Lastly, FWM is a third-order nonlinear optical effect which leads to efficient generation of new optical frequencies if phase matching condition is satisfied. All of these mechanisms play a key role in the design of dual-seed optical comb sources.

2.1.1 Group Velocity Dispersion (GVD)

The propagation of short pulses in optical fibers is affected by dispersion. To understand fiber dispersion, we consider the propagation constant, $\beta(\omega)$, which is frequency dependent. A Taylor series expansion of the propagation constant about a central frequency, ω_0, associated with the pulse can be written as

$$\beta(\omega) = \beta(\omega_0) + \beta_1(\omega - \omega_0) + \frac{\beta_2}{2}(\omega - \omega_0)^2 + \cdots \tag{2.1}$$

where

$$\beta_1 = \left(\frac{d\beta}{d\omega}\right)_{\omega=\omega_0} = \frac{1}{v_g} \tag{2.2}$$

$$\beta_2 = \left(\frac{d^2\beta}{d\omega^2}\right)_{\omega=\omega_0} \tag{2.3}$$

and v_g is the group velocity. For the short pulse that propagates along an optical fiber of length L, a spectral component arrives at the fiber output with a time delay $\tau = L/v_g$.

If $\Delta\omega$ is the spectral width associated with the pulse, it means different spectral components are present within this finite spectral range. From Eq. (2.2), the group velocity varies with optical frequency. Therefore, different frequencies composing the pulse travel at different speeds and arrive at the fiber end at different times. In other words, the frequency-dependent group velocity causes the pulse to spread in time, and the pulse broadening can be calculated as [24]

$$\Delta\tau = \frac{d\tau}{d\omega}\Delta\omega = \frac{d}{d\omega}\left(\frac{L}{v_g}\right)\Delta\omega = L\beta_2\Delta\omega \tag{2.4}$$

This pulse broadening due to the frequency-dependent group velocity is called group velocity dispersion (GVD). In Eqs. (2.3) and (2.4), the second-order derivative, β_2, is referred to as the GVD parameter. In practice, fiber dispersion also can be expressed in terms of a dispersion parameter D, which is linked to β_2 by

$$D = -\frac{2\pi c}{\lambda^2}\beta_2 \tag{2.5}$$

where λ is wavelength, and the unit for dispersion parameter D is ps/nm/km. For both linear and nonlinear regimes, an important value is the zero-dispersion wavelength (ZDW) at which β_2 and D vanish. In a standard single-mode fiber (SMF), the typical zero-dispersion wavelength is around 1310 nm.

For positive β_2 (negative D) which corresponds to normal dispersion, low-frequency (long-wavelength) components of a short pulse travel faster. For negative β_2 (positive D) which represents anomalous dispersion, by contrast, higher frequencies (shorter wavelengths) in a pulse travel faster. As a result, the sign of GVD parameter (or dispersion parameter) determines the distribution of spectral components in an optical pulse. Explicitly speaking, low-frequency components occupy the leading edge of the pulse for normal dispersion, while high-frequency components distribute over the leading edge of the pulse for anomalous dispersion.

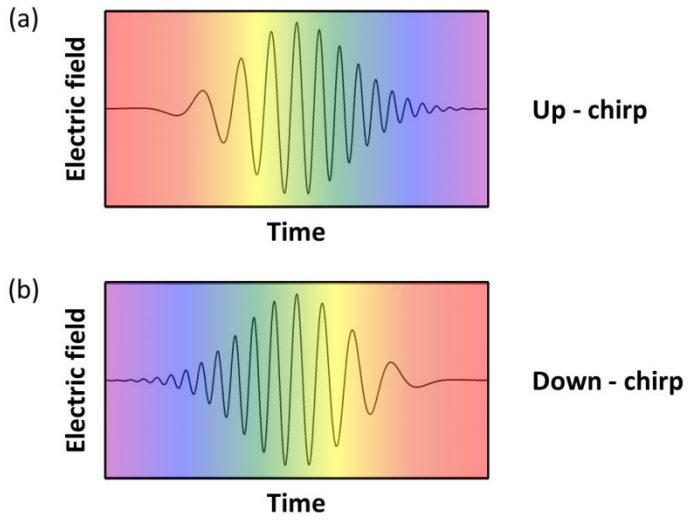

Fig. 2.1 The linearly chirped pulses. (a) up-chirp represents the frequency linearly increases with time, and (b) down-chirp means the frequency linearly decrease with time.

2.1.2 Compression of Linearly Chirped Pulses

A pulse is said to be chirped if this pulse has an instantaneous frequency which varies as a function of time. Specifically, we focus on a linearly chirped pulse in which the frequency linearly varies with time. Figure 2.1 exhibits two possible cases of linearly chirped pulses including a positively chirped pulse (up-chirp) and a negatively chirped pulse (down-chirp). In Fig. 2.1(a), the frequency associated with a positively chirped pulse increases linearly with time. In Fig. 2.1(b), for a negatively chirped pulse, the frequency decreases linearly from the rising to the falling edge.

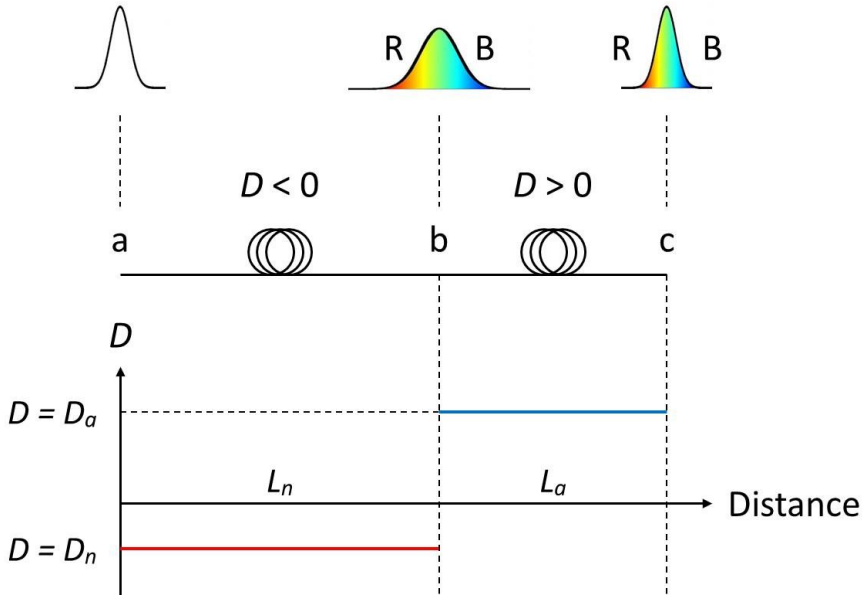

Fig. 2.2 Compression of a chirped pulse. At position *a*, an initially unchirped pulse is sent into an optical fiber with a negative dispersion parameter. At position *b*, the pulse becomes positively chirped, and the blue-component (B) appears behind the red-component (R) due to the normal dispersion. Next, the chirped pulse propagates along an optical fiber with a positive dispersion parameter. The blue-component travels faster and the red-component becomes slower due to the anomalous dispersion. Thus, the chirped pulse can be compressed at position *c*.

Further, according to the aforementioned discussion on normal and anomalous dispersion, the width of a chirped pulse can be properly regulated by varying the sign of GVD parameter or dispersion parameter in a fiber link. Figure 2.2 shows an example which illustrates a chirped pulse compression by means of insertion of different fiber with an opposite sign. At the input of the link (position a), an initially unchirped pulse is sent into an optical fiber with normal dispersion D_n (negative dispersion parameter) and length L_n. Due to the normal dispersion, at the end of this span of fiber (position b), the pulse spreads in time and the low-frequency component marked R appears before the high-frequency component marked B, which leads to a dispersion-induced chirp. Following, the positively chirped pulse enters into the second spool of fiber with anomalous dispersion D_a (positive dispersion parameter) and an optimized length L_a. Now, due to the anomalous dispersion, the high-frequency component travels faster and catches up, while the travel time of the low-frequency component is longer. Thus, at the output of the fiber link (position c), the chirped pulse can be compressed to a minimum width by choosing a spool of fiber with an opposite sign and an optimized length. Importantly, the pulse broadens again beyond the optimized length, so the fiber used for compression should be tailored carefully.

2.1.3 Four Wave Mixing (FWM)

The generation of a dual-seed optical comb source also relies on a nonlinear optical technique known as four-wave mixing (FWM). This nonlinear optical effect

originates from the presence of the third-order susceptibility $\chi^{(3)}$. Four-wave mixing is a parametric process during which pump waves and a signal wave interact with each other in a third-order nonlinear medium to create an idler wave at a new frequency. Accordingly, energy of pump waves is transferred to signal and idler waves. In the wave-mixing interactions, energy and momentum must be conserved, and the conservation of momentum results in the phase matching condition. Note that the wavelength of pumps involved in the process should be close to the zero-dispersion wavelength of the nonlinear medium to fulfill the requirement for the phase matching condition and thus enhance the FWM efficiency [25].

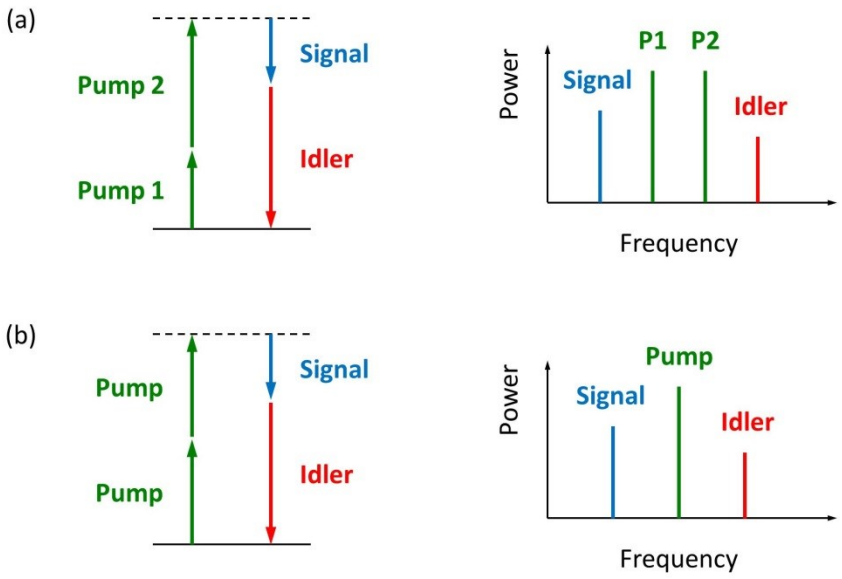

Fig. 2.3 Four-wave mixing (FWM). This wave-mixing process can be (a) a non-degenerate FWM where two pump photons of different frequencies mix with a signal photon to produce a new idler photon, and (b) a degenerate FWM where two pump photons with identical frequency and a signal photon mix to create an idler photon. In both cases, the energy diagram showing conservation of energy is on the left (dash line represents the virtual energy level), and the corresponding spectrum is on the right.

Basically, four-wave mixing can be classified into two categories, namely non-degenerate and degenerate FWM, as seen in Fig. 2.3. For both cases of FWM, a new component, idler, is generated and its frequency and phase are related to the pumps and signal involved in the process. In non-degenerate FWM described by Fig. 2.3(a), two pump photons with different frequencies ω_{p1} and ω_{p2} and a signal photon at ω_s mix to generate an idler photon at ω_{idler}. In the spectrum, each of the pump sources provides a photon and there are two pump lines at the middle. The electric field amplitude and frequency of the newly generated idler wave are

$$E_{idler} \propto E_{p1}E_{p2}E_s^* \tag{2.6}$$

$$\omega_{idler} = \omega_{p1} + \omega_{p2} - \omega_s \tag{2.7}$$

where the symbol "*" denotes complex conjugate. Figure 2.3(b) illustrates the process of degenerate FWM (also called partially-degenerate or pump-degenerate FWM) in which two pump photons with an identical frequency ω_p and a signal photon at ω_s mix to create an idler photon. In the spectrum, there is only one pump line since this pump source can provide two photons. Now, the created idler wave possesses electric field amplitude and frequency

$$E_{idler} \propto E_pE_pE_s^* \tag{2.8}$$

$$\omega_{idler} = 2\omega_p - \omega_s \tag{2.9}$$

In general, the FWM process for both non-degenerate and degenerate cases has a very low efficiency due to a phase mismatch. In a given third-order nonlinear medium, the FWM efficiency can be improved by adjusting wavelengths and power

of the participating waves. As mentioned previously, the wavelength of pump(s) should be located near the zero-dispersion wavelength. On the other hand, a proper pump power can give a required nonlinear phase shift to balance the dispersion effect of the medium.

2.2 Principle of Operation and Limitations

The first part of this section is devoted to the discussion on the architecture and principle of dual-seed optical comb sources. Each stage in the multi-stage structure is responsible for various tasks. Following, implementation challenges in the realization of this parametric device are introduced in the second part. These limitations include the power saturation due to stimulated Brillouin scattering (SBS) and the fluctuation of zero-dispersion wavelength along optical fibers.

2.2.1 Architecture and Principle

In the architecture of a dual-seed optical comb source (OCS), two continuous-wave (CW) laser sources are used as seeds to induce a chirp-compression-mixing process in cascaded stages of highly-nonlinear fiber (HNLF) separated by a tailored single-mode fiber (SMF) which can compress the temporal waveform [26,27]. When sufficient power is injected into the multi-stage device, newly generated FWM products will be built up and continue to trigger high-order tones.

Figure 2.4 shows the architecture and principle of a dual-seed optical comb source [27]. Two CW lasers serve as seeds to initiate chirp-compression-mixing

processes. The two seeding waves at wavelengths of λ_1 and λ_2 are first combined and amplified by an Erbium-doped fiber amplifier (EDFA), and then these two tones beat and enter a first stage of highly-nonlinear fiber ($HNLF_1$) used to induce a chirp and initiate a limited multi-tone generation. In practice, both seeds should be close to the zero-dispersion wavelength of the $HNLF_1$ due to the requirement for phase matching. In the following stage, a tailored SMF can compress the chirped waveform in the temporal domain to enhance the peak power (see Section 2.1). Subsequently, the compressed waveform with higher peak power is injected into the last stage ($HNLF_2$), enabling this nonlinear stage to generate a multitude of high-order tones due to FWM.

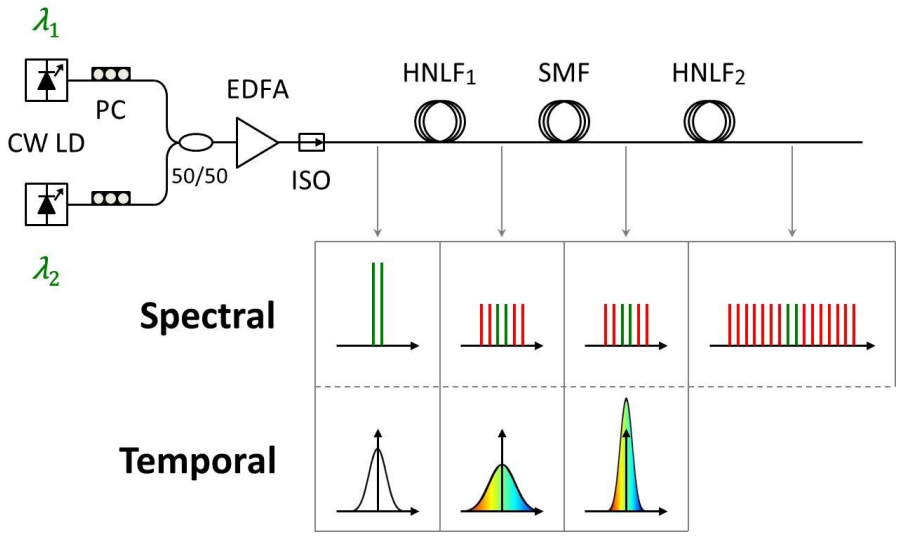

Fig. 2.4 Generation of a dual-seed optical comb source. Two CW lasers at λ_1 and λ_2 are first combined and amplified, and then sent into cascaded stages of optical fibers. A comb spectrum is generated by a chirp-compression-mixing process. CW LD: continuous-wave laser diodes, PC: polarization controller, 50/50: 3-dB optical coupler, EDFA: erbium-doped fiber amplifier, ISO: optical isolator, HNLF: highly-nonlinear fiber, and SMF: single-mode fiber.

Note that the comb spacing between adjacent spectral components for the generated dual-seed optical comb source is determined by the wavelength (frequency) spacing between the two seed laser sources due to the parametric (FWM) process. In other words, this type of frequency comb source is a suitable candidate for wavelength-division multiplexing (WDM) applications in which a channel spacing of 0.8 nm (100 GHz grid) or 0.4 nm (50 GHz grid) is desired.

2.2.2 Implementation Challenges

Two pivotal keys to the efficient generation of dual-seed optical comb sources are suppression of the stimulated Brillouin scattering and mitigation of the zero-dispersion wavelength fluctuation along the optical fibers. The SBS effect limits the maximum power that can be launched into optical fibers to induce the parametric processes, while the fluctuation of zero-dispersion wavelength degrades the efficiency and bandwidth of the comb spectrum by destroying the phase-matching condition.

First, the length of $HNLF_1$ should be short enough since the SBS sets the corresponding maximal power that can be transmitted through the fiber with a given length. For example, for a 100-m long $HNLF_1$ with a nonlinear coefficient (γ) of 11.3 $W^{-1}km^{-1}$, the output power at the end of $HNLF_1$ reaches power saturation due to the backward reflection caused by SBS (Fig. 2.5, black). Alternatively, a long $HNLF_1$ can transmit power without saturation by applying a proper tension plan along the optical fiber to modify the SBS frequency and increase the SBS threshold

[28,29]. In our work, a longitudinally varying strain plan with 10-step stair-ramp distribution is applied, and therefore the transmitted power at the output of $HNLF_1$ linearly increases with the injected power (Fig. 2.5, red).

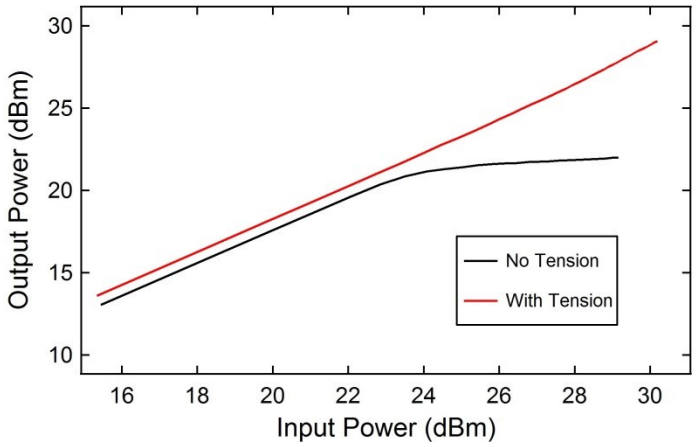

Fig. 2.5 Power limitation due to stimulated Brillouin scattering (SBS). Black curve: 100-m HNLF without tension plan suffers from SBS limitation. Red curve: 100-m HNLF with tension plan averts SBS limitation.

Second, due to the phase matching requirement, both seed wavelengths are aligned to the zero-dispersion wavelength which is expected to remain constant over the entire optical fiber. However, unavoidable microscopic geometry imperfections result in ZDW fluctuations that lead to bandwidth reduction of the dual-seed optical comb source. Although the aforementioned longitudinally varying tension plan is designed for SBS suppression, note that a proper tension map is also able to equalize the ZDW fluctuation along the optical fiber. This spatial equalization of ZDW profile enabled by stretching fibers allows the bandwidth enhancement of the parametric device [30].

2.3 Experimental Demonstration

The limitations for implementing a dual-seed optical comb source have been introduced in the previous section. Those challenges including a low SBS threshold and a large zero-dispersion wavelength fluctuation must be overcome. In the first half of this section, the improvement brought by a tension plan is validated. Next, the generated optical spectra of our dual-seed optical comb sources are given in the second half of this section.

2.3.1 Improvement by a Tension Plan

In an entire architecture of the dual-seed optical comb source, the first stage of highly-nonlinear fiber ($HNLF_1$) is responsible for inducing a chirp and initiating a parametric process. If more tones are generated by this first nonlinear stage (and the chirped pulses are compressed by a linear stage), it can be expected to trigger a multitude of comb components at the output of the last nonlinear stage ($HNLF_3$) due to the various FWM products in the parametric process. Hence, we focus our attention on a single stage of highly-nonlinear fiber ($HNLF_1$), and the goal is now aimed to the efficient multi-tone generation by means of a longitudinally varying strain plan.

The first sample used here is a 100-m long highly-nonlinear fiber with a nonlinear coefficient of 11.3 $W^{-1}km^{-1}$, and the wavelength spacing between two seed lasers is set to 1.6 nm (200 GHz at 1550 nm region). The two seeding waves are combined and amplified by an EDFA which is set at 1.5 W. If the optical fiber

without being added any tension plan is utilized, only a few FWM idlers with low conversion efficiency can be created (see black dash curve in Fig. 2.6(a)). By contrast, under the same conditions, some additional higher-order tones emerge once a designed 10-step stair-ramp tension plan is applied to the optical fiber (see red solid curve in Fig. 2.6(a)).

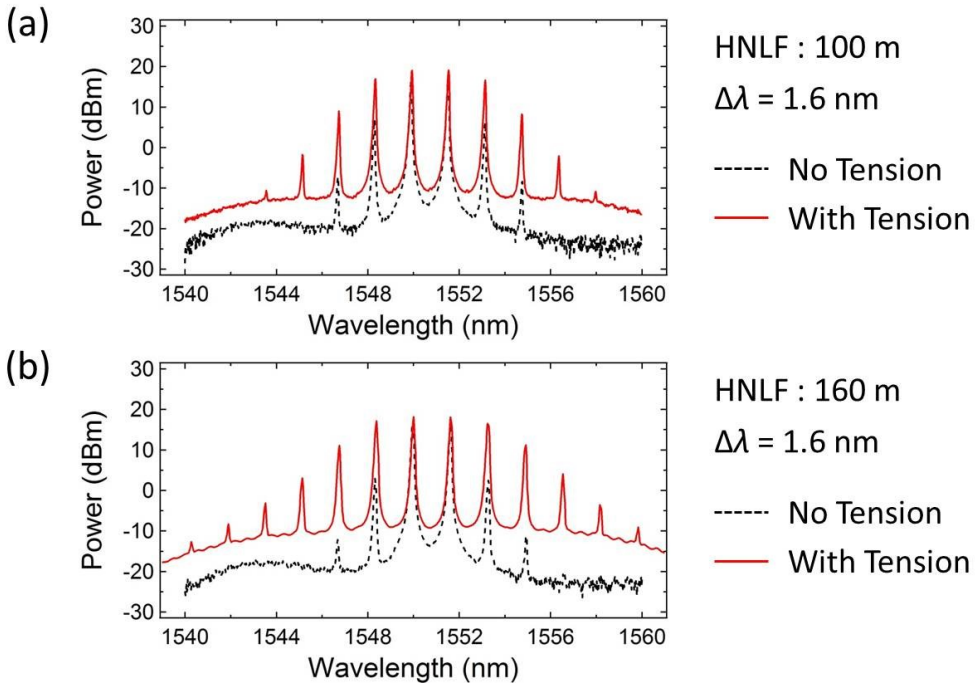

Fig. 2.6 Optical spectra showing the improvement by a strain plan. Two samples include (a) 100-m long HNLF and (b) 160-m long HNLF. In both cases, the black dash curves represent that untensioned HNLFs result in limited tones, while the red solid curves show that tensioned HNLFs lead to an increased bandwidth.

As a second sample, the 100-m long optical fiber is replaced by a 160-m long highly-nonlinear fiber with the same parameters, and the wavelength and power setting is kept the same as that used for the previous sample. As seen in the Fig. 2.6(b), the black dash curve indicates still limited tones with poor conversion

efficiency are generated by an ordinary fiber without any strain plan. Here, it is meaningful to compare the spectra for both untensioned samples (both black dash curves in Fig. 2.6(a) and (b)). From the two cases, the number of generated FWM idlers is not increased with the interaction length, indicating the stimulated Brillouin scattering limits the generation of new FWM idlers. Following, the aforementioned longitudinal varying tension distribution is still applied to this sample, and each step along the fiber for the strain plan correspondingly becomes longer. In this tensioned case, more higher-order tones appear through the parametric process, as shown by the red solid curve in Fig. 2.6(b).

Therefore, the longitudinally tensioned highly-nonlinear fiber benefits the implementation of a dual-seed optical comb source since more tones can be generated at this first nonlinear stage. These newly developed tones can further trigger higher-order comb components through the parametric process as long as the chirped pulses are effectively compressed in the next linear stage.

2.3.2 Results and Discussion

Fig. 2.7 presents the measured optical spectra of two sets of dual-seed optical comb sources with 0.4 and 1.6 nm comb line spacing, respectively. In the optical comb source with 0.4 nm spacing between adjacent comb lines (Fig. 2.7(a)), the lengths of $HNLF_1$ and $HNLF_2$ are 100 and 160 m, and SMF length is 400 m. The above-mentioned 10-step stair-ramp strain plan is applied to both $HNLF_1$ and $HNLF_2$ which possess a nonlinear coefficient of 11.3 $W^{-1}km^{-1}$. For the other comb

source with 1.6 nm spacing (Fig. 2.7(b)), both nonlinear stages of $HNLF_1$ and $HNLF_2$ remain exactly the same as that in the device with 0.4 nm comb spacing, but the length of SMF used as a compressor is decreased to 23 m for optimal compression.

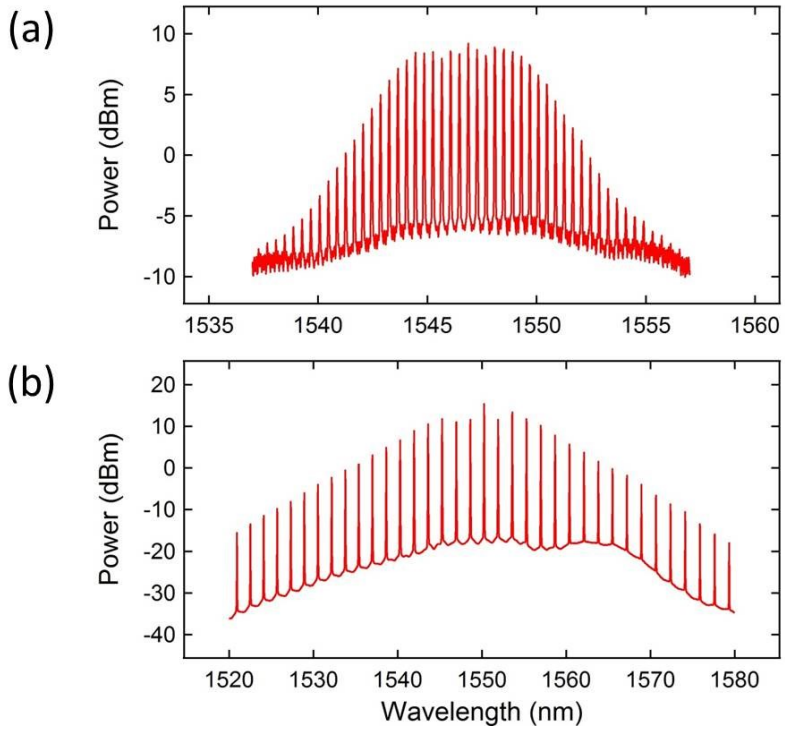

Fig. 2.7 Measured optical spectra for two sets of dual-seed optical comb sources with (a) 0.4 nm and (b) 1.6 nm wavelength spacing. Resolution of optical spectrum analyzer is 0.05 nm.

For some applications, an optical frequency comb which possesses an octave-spanning bandwidth is desirable. In the scheme of dual-seed optical comb sources, by adding more compression and mixer stages, multiple chirp-compression-mixing cycles can further generate more comb components to enhance the bandwidth. Additionally, spectrum flatness is also important for some applications where power equalization between comb lines can greatly enhance the system performance. To

this end, sidelobes of the compressed temporal pulse at the SMF compressor can be rejected with the aid of nonlinear optical loop mirror (NOLM), enabling spectral flatness over an ultra-wide band [31].

2.4 Comparison with Other Counterparts

In addition to the MLL-based optical frequency combs (see Chapter 1) and the dual-seed optical comb sources discussed in this chapter, another two types of optical frequency combs are also attractive. They are modulator-based and microresonator-based frequency combs. Importantly, due to diverse demand, each of the above four categories of frequency combs possesses its own features to fit in various applications. Hence, the desirable and ideal features of an optical frequency comb depend on the purpose and function of the application.

2.4.1 Modulator-based Combs

The structure of a modulator-based frequency comb generator [18,19] generally consists of a CW laser source and a phase modulator, as exhibited in Fig. 2.8. The CW carrier provided by a narrow-linewidth laser is injected into a phase modulator driven by an RF oscillator to produce wide sidebands. The generation of wide sidebands associated with the phase-modulated light represents that the chirped light contains a spectrum of spectral components, and this function is similar to that given by the first stage of highly-nonlinear fiber in the dual-seed optical comb sources. For a dual-seed optical comb source, a large number of spectral

components created by the first stage of nonlinear medium are also desirable. However, in this modulator-based scheme, the sideband width is proportional to the modulation index of the modulator [18], so a large modulation index is required for achieving a wide sideband. In this scheme, the central frequency is determined by the CW laser source and the comb spacing between adjacent spectral components is defined by the modulation frequency (oscillator frequency).

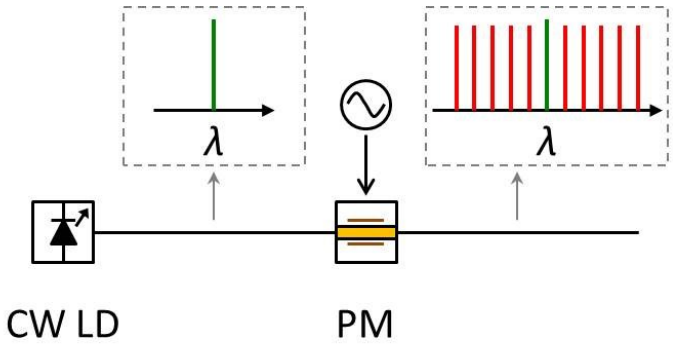

Fig. 2.8 A modulator-based optical frequency comb. A CW light with a narrow linewidth is launched into a phase modulator to induce a chirp and produce sidebands. Consequently, a spectrum of comb components can be generated in frequency domain. CW LD: continuous-wave laser diode, PM: phase modulator.

Evidently, the key to this approach is the phase modulator which dominates bandwidth and frequency spacing of the generated frequency comb. First, as mentioned above, the phase modulator is responsible for inducing a broad sideband and leading to a generation of spectral comb lines, but the generation of a wide bandwidth requires a large modulation index. This means a phase modulator which possesses a low half-wave voltage (V_π) and an ability to handle high RF power is desired [19]. Alternatively, the bandwidth can be expanded by either cascading a

series of modulators [19] or adding an additional highly-nonlinear fiber to generate more tones through four-wave mixing [32]. Second, as introduced previously, the modulation frequency (oscillator frequency) determines the frequency spacing of the comb spectrum. In other words, the bandwidth of the phase modulator (and the RF oscillator) imposes a limit to the frequency spacing of the generated comb spectrum. Currently, maximum bandwidth of a commercial lithium niobate modulator is around 40 GHz, and thus the limited bandwidth of a modulator restrains the scalability of comb spacing.

2.4.2 Microresonator-based Combs

Optical frequency combs can also be achieved through the cascaded four-wave mixing process in a high-Q nonlinear optical microresonator, as shown in Fig. 2.9. A tunable CW pump laser is aligned to a resonance mode of the micro-cavity, and neighbor modes obtain optical gain through the parametric amplification. These participated modes gradually build up and give rise to oscillation. Subsequently, the high intensity within the microresonator triggers degenerate four-wave mixing between the pump and different oscillating frequencies. The newly generated spectral components can further interact with each other through non-degenerate four-wave mixing to create a multitude of higher-order comb components [21,23].

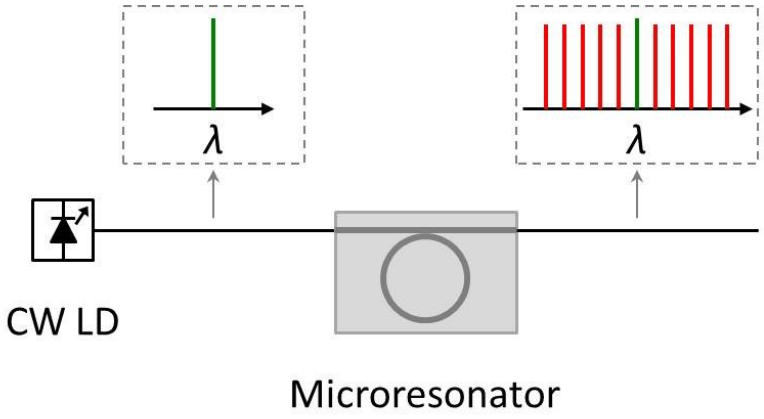

Fig. 2.9 A microresonator-based optical frequency comb. A CW pump is aligned to a resonant mode of the microresonator, and adjacent modes acquire gain through parametric amplification. The pump wave and these oscillating modes interact with each other through cascaded four-wave mixing to span a wide comb spectrum.

It is known that an efficient four-wave mixing process relies on high waveguide nonlinearity, sufficient pump intensity, long interaction length, and phase match. From this perspective, microresonator-based combs are promising. Different materials with high nonlinearity are recently used for fabrication of these devices. Moreover, microresonators can confine optical field in a small area and result in the enhancement of optical intensity and nonlinear interaction. Importantly, precise dispersion engineering by a proper design of waveguide cross-section plays a critical role in the design of microresonator-based combs since dispersion in the nonlinear medium forces the present modes to vary with wavelength [21,22].

2.4.3 Comparison between Four Types of Combs

So far, four types of optical frequency combs have been discussed, and this optical frequency comb family includes (1) MLL-based, (2) modulator-based, (3) microresonator-based, and (4) dual-seed optical comb sources. All of these various categories of frequency combs can find proper applications in diverse areas such as spectroscopy, metrology, astronomy, and telecommunications or signal processing. Here, this part is focused on the discussion on the frequency spacing between successive spectral lines for each type of frequency combs.

First, the repetition rate for the MLL-based comb is relatively low due to the limitation on cavity length, and the repetition rate is typically lower than 10 GHz. The combination of features including low repetition rate and high accuracy make this type of frequency comb suitable for the applications in spectroscopy and metrology. As aforementioned, the frequency spacing of modulator-based combs is limited by the RF oscillator frequency and the bandwidth of modulators, and the maximum bandwidth of a current commercial phase modulator is around 40 GHz. This kind of frequency combs is a suitable candidate for optical arbitrary waveform generation [5].

For current wavelength-division-multiplexing (WDM) applications, the channel spacing is 50 GHz or 100 GHz. The microresonator-based and dual-seed optical comb sources are both able to satisfy the demand for channel requirement. These two types of frequency combs basically share the underlying principle since they both utilize four-wave mixing to generate a multitude of comb components. For the

microresonator-based comb, the frequency spacing is related to the device size, and the spacing covers a wide range from 10 to 1000 GHz [33]. The dual-seed optical comb sources also can achieve a large frequency spacing since the spacing is defined by the frequency separation between two seed laser sources, but their wavelengths must be close to the zero-dispersion wavelength of the optical fibers. Table 2.1 gives a brief summary of the four types of optical frequency combs.

	Device/Principle	Comb spacing →	Limited by
MLL-based	Mode-locked laser	< 10 GHz	Cavity length
Modulator-based	Phase modulator	10 - 40 GHz	Modulator bandwidth
Microresonator-based	Four-wave mixing	10 – 1000 GHz	Size
Dual-seed	Four-wave mixing	Tens to hundreds of GHz	Phase matching

Table 2.1 Comparison between four types of optical frequency combs including MLL-based, modulator-based, microresonator-based, and dual-seed optical comb sources.

Chapter 3

Wavelength Multicasting

The functionality of wavelength multicasting enables numerous replicas of an input data-carrying signal at distinct output wavelengths. Figure 3.1 illustrates an application of wavelength multicasting in a wavelength-division-multiplexing (WDM) network. In the network, a sender delivers only one packet at a certain wavelength λ_s. This data is first duplicated, and the replicas are sent to multiple specific destinations so that part of different users in the network can simultaneously receive the data at assigned wavelengths (see users in red). A requirement for wavelength multicasting is the generation of a number of replicas.

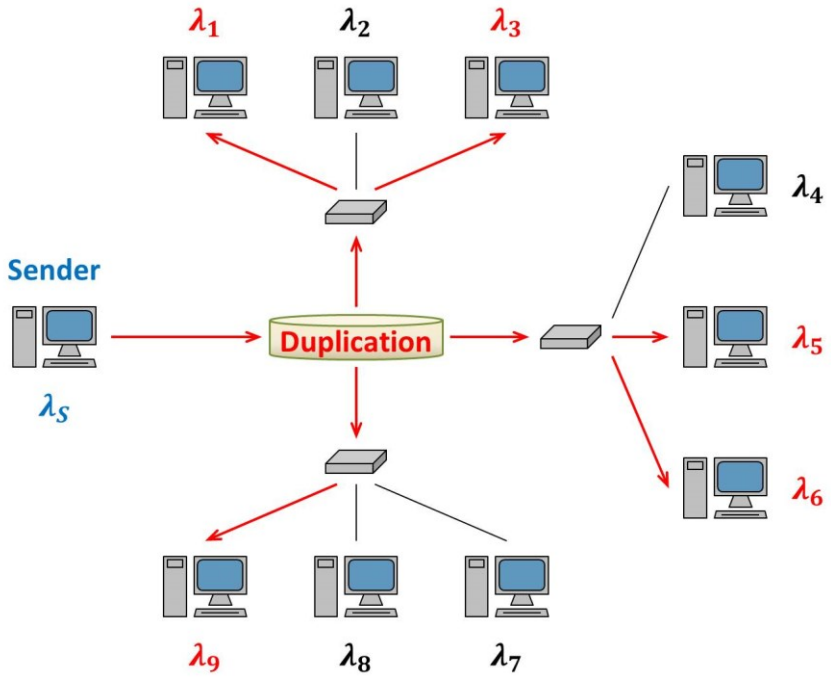

Fig. 3.1 An application of wavelength multicasting in a wavelength-division-multiplexing (WDM) network. Data from the sender must be duplicated, and then the copies are sent to part of users in the network at assigned wavelengths.

3.1 Introduction

Wavelength multicasting is an indispensable tool in an optical network for efficient simultaneous delivery of a data stream from one single element to a group of destinations [34-36]. Additionally, the parallelism afforded by wavelength multicasting makes this operation essential to a variety of ultrahigh-speed optical signal processing systems [37-41]. For example, demonstrated applications based on wavelength multicasting include a channelized radio-frequency receiver [39], an optical tapped delay line [40], and serial-to-parallel conversion [41]. The critical challenge in efficient multicasting is to provide a multitude of high-quality channels

while minimizing the needed resources. Various approaches to wavelength multicasting have been demonstrated through several nonlinear optical effects in diverse devices. In addition to the four-wave mixing (FWM) process used here, these approaches include cross-phase modulation (XPM) in a silicon nanowire [42], cross-gain modulation (XGM) in a semiconductor optical amplifier (SOA) [43], cross-absorption modulation (XAM) in an electroabsorption modulator (EAM) [44,45], and self-phase modulation (SPM) in a photonic-crystal fiber (PCF) [46].

FWM is a desirable mechanism for achieving wavelength multicasting as the generated FWM idlers inherently enable wavelength conversion of a signal. An early on-chip demonstration by Biberman *et al.* showed 16-way wavelength multicasting through degenerate FWM in a silicon waveguide by mixing an on-off keying (OOK) data-encoded partially-degenerate pump with an array of 16 continuous wave (CW) laser sources [47]. Each CW laser source mixed with the OOK encoded pump to provide an individual idler carrying the OOK data from the pump [47,48]. However, this approach requires a large number of individual laser sources and is not modulation format transparent due to the use of a data-carrying degenerate pump, which, for example, will non-linearly transfer phase modulation to the multicast signals. More recently, FWM generation of phase preserving replicas has been investigated through dual-pump FWM that uses two individual CW laser sources as the pumps and the data-carrying wave as a seed signal to obtain six multicast channels [49]. Adding more CW pump lasers allows this basic approach to generate a larger number of multicast channels [50]. However, in addition to being resource intensive, a non-uniform pump wavelength spacing is required to avoid noisy

interference among the phase incoherent but spectrally coincident FWM idlers due to the phase incoherence of the array of free-running pump lasers [50,51].

Rather than using multiple independent lasers, comb sources generated using optical parametric processes efficiently provide a multitude of pump lines suitable for multicasting operations [52,53]. For example, more than 60 phase-preserved multicast channels can be achieved by using higher-order mixing processes in a dual-pump parametric mixer with compression/mixing stages [53]. In this existing approach, only two CW pump waves and a data-carrying signal wave are combined and injected into the compression/mixing stages leading to the efficient generation of numerous multicast channels through cascaded FWM. However, using this approach the multicast channels are interleaved with the replicas of pumps, and therefore this scheme requires a corresponding filter arrangement to reject the unused pumps. More importantly, this approach requires highly cascaded FWM of a wide-bandwidth data-carrying signal making it difficult to implement in, for example, chip-scale devices. While highly cascaded FWM has been demonstrated in microresonator-based devices [22], the narrow resonance bandwidth required to achieve sufficient resonant enhancement of the FWM process makes these devices unable to accommodate a high-speed signal in the interaction.

3.2 Principle

For FWM-based wavelength multicasting, adding more pump waves yields a greater number of generated idlers. Here we use uniformly spaced lines from a dual-

seed optical comb source which serve as both degenerate and non-degenerate pump waves in mixing with an input signal to generate a multitude of idlers. These idlers represent the wavelength multicast replicas of the signal and the approximate number of replicas is given by the relation $n = 4m - 3$, where m is the number of pump waves (comb lines) used in the FWM processes and n is the number of generated multicast replicas.

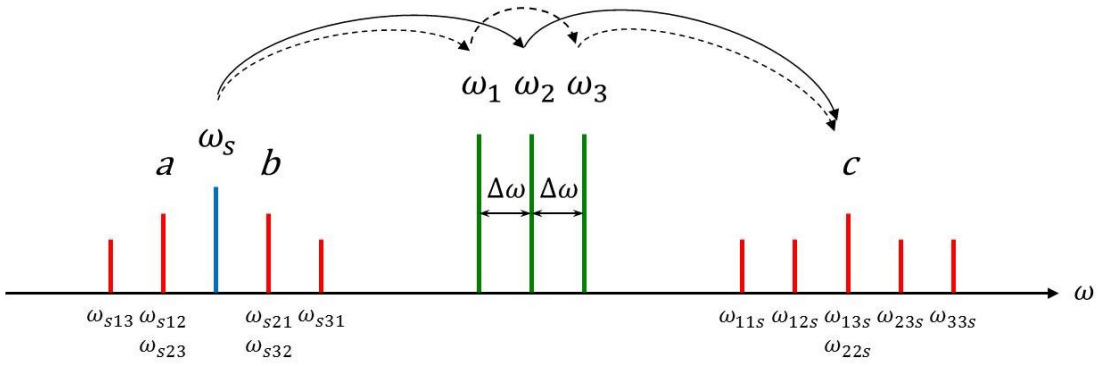

Fig. 3.2 An illustration of spectrally coincident FWM products. Given three uniformly-spaced pumps (in green) and an input signal (in blue), nine multicast replicas (in red) carrying the original input signal are generated. Among these replicas, each of *a*, *b*, and *c* consists of multiple FWM products at a coincident frequency. For example, two FWM products, ω_{13s} (dash) and ω_{22s} (solid), both contribute to the replica *c*. If the pump waves are provided by independent free-running lasers, then the multiple FWM pathways will lead to noisy interference and thus poor multicast signal quality.

For many of these generated idlers multiple FWM pathways exist for their generation as depicted in Fig. 3.2. To illustrate this effect, we denote the frequencies of the three uniformly-spaced pump waves and the input signal wave shown in Fig. 3.2 as ω_1, ω_2, ω_3, and ω_s, respectively. Each newly generated wave via FWM process can be expressed as $\omega_{ijk} = \omega_i + \omega_j - \omega_k$, where *i*, *j*, and *k* indicate three waves participating in the FWM process. The corresponding spectral phase of the FWM

generated wave is represented by $\varphi_{ijk} = \varphi_i + \varphi_j - \varphi_k$, where φ_i, φ_j, and φ_k are the spectral phases of the three waves involved in the process. In this example case (m = 3), ten multicast data-carrying idlers (including the output signal at ω_s and nine replicas) are generated.

Importantly, each of the newly generated replicas *a*, *b*, and *c* results from spectrally coincident contributions from distinct FWM pathways. For example, the replica *c* is the result of the two pathways depicted in Fig. 3.2 with coincident frequencies at ω_{13s} and ω_{22s}. The spectral phases of these two components are $\varphi_{13s} = \varphi_1 + \varphi_3 - \varphi_s$ and $\varphi_{22s} = 2\varphi_2 - \varphi_s$, respectively. For ideal constructive interference these two spectral phases, φ_{13s} and φ_{22s}, should be equal indicating that a linear phase relationship amongst the pump waves $\varphi_1 + \varphi_3 = 2\varphi_2$ is desired. Most critically, if the relative phase of the pump waves is not fixed, as is the case for independent CW pump lasers, the relative phase noise will lead to noisy interference from the multiple FWM pathways resulting in loss of the data quality in the multicasting process. Therefore, it is crucial that the pump waves possess a fixed (preferably linear) phase relationship as is the case for the optical comb source used here.

3.3 Experimental Setup

Figure 3.3 depicts the multicasting architecture used for differential phase-shift keying (DPSK) demonstration. A dual-seed optical comb source provides pump waves with a fixed relative phase relationship. In this optical comb source, two independent CW lasers with a wavelength spacing of 0.4 nm are combined by a 3-dB

coupler, amplified by an erbium-doped fiber amplifier (EDFA), and sent into two cascaded FWM stages separated with a designed length of single-mode fiber (SMF) used for temporally compressing the generated pulses after the first FWM stage [27,53]. The lengths of two segments of HNLFs which serve as the FWM stages are 100 and 160 m, respectively, and the SMF length is 400 m.

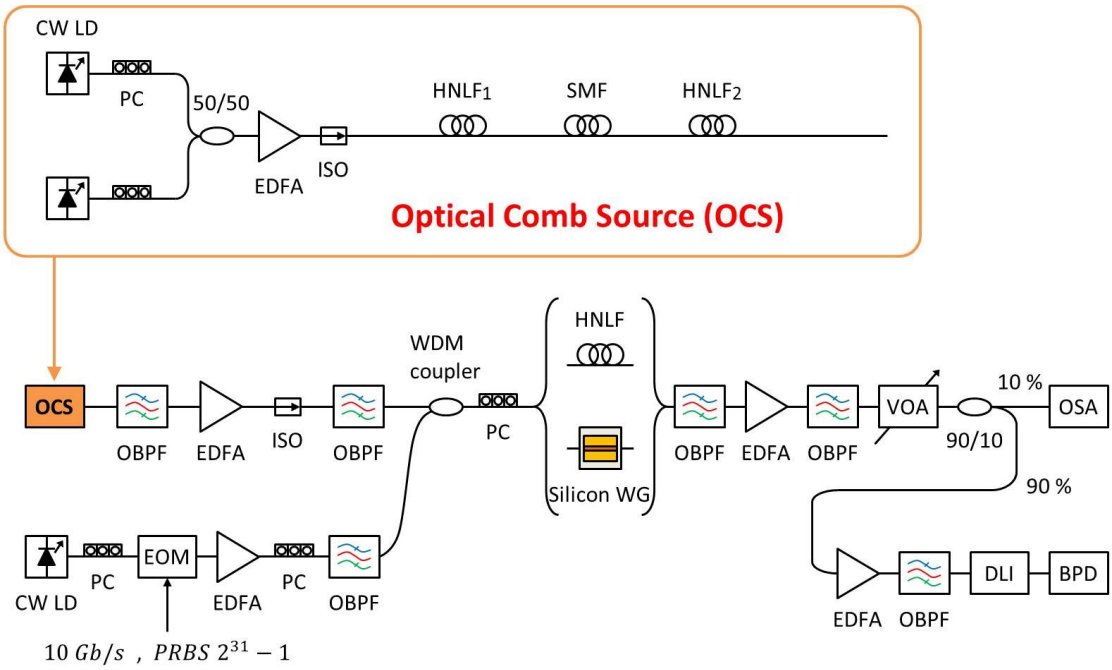

Fig. 3.3 Experimental setup of the proposed wavelength multicasting scheme using a dual-seed optical comb source. CW LD: continuous-wave laser diode, PC: polarization controller, EDFA: erbium-doped fiber amplifier, ISO: optical isolator, HNLF: highly-nonlinear fiber, SMF: single-mode fiber, OCS: optical comb source, OBPF: optical band-pass filter, EOM: electro-optic modulator, Silicon WG: silicon waveguide, VOA: variable optical attenuator, OSA: optical spectrum analyzer, DLI: delay interferometer, and BPD: balanced photodetector.

To enhance the mixer bandwidth, a longitudinally varying tension plan [27-30] with 10-step stair-ramp distribution is applied to both HNLFs (OFS, with nonlinear coefficient of 11.3 $W^{-1}km^{-1}$, and a dispersion parameter of 1.93 ps/nm/km at 1550

nm). The total power at the output of the optical comb source is 480 mW. This process leads to the generation of a large number of equidistant spectral lines through cascaded FWM.

The adjacent lines from the optical comb source are spectrally isolated by a tunable optical band-pass filter (OBPF) for use as pump waves for the multicasting stage. These pump waves are amplified by an EDFA, and then filtered by a 5.3-nm OBPF to remove the amplified spontaneous emission (ASE) noise introduced by the EDFA. The pump power injected into the HNLF and the silicon waveguide is 607 mW and 36.5 mW, respectively; the optical signal-to-noise ratio (OSNR) of pump is measured to be 41.2 dB. The signal wave is produced by another CW laser at 1558.98 nm, which is modulated in a lithium niobate electro-optic modulator (EOM) with a 10-Gb/s DPSK signal encoded by a $2^{31} - 1$ pseudo-random binary sequence (PRBS). The data-carrying signal wave is amplified by an EDFA, filtered by a narrow-band OBPF, and then combined with the pump waves using a WDM coupler with a 9-nm passband. In the signal (lower) branch, the power at the output of the CW laser and the EOM is 1.5 mW and 0.7 mW, respectively, and the power after the signal EDFA is 150 mW for the HNLF and 260 mW for the silicon waveguide, respectively; the signal OSNR is measured to be 45.9 dB. After being combined, the total power including pumps and signal into the HNLF and the silicon waveguide is 660 mW and 44 mW, respectively. Subsequently, these pump waves and the signal wave mix through FWM in either a 30-m long HNLF (OFS, with nonlinear coefficient of 11.5 $W^{-1}km^{-1}$, a dispersion parameter of 0.1 ps/nm/km at 1550 nm, and a zero dispersion wavelength of 1543 nm) or a 15-mm long silicon waveguide (described

below) leading to the generation of a multitude of wavelength multicast replicas of the signal. The total power at the output of the multicasting stages is 550 mW for the HNLF and 2.4 mW for the silicon waveguide, respectively.

To validate the BER performance for each multicasting channel, an OBPF is used to reject the pump waves. All of the multicast channels are then amplified and each channel is isolated by a narrow-band tunable OBPF. Finally, the selected individual channel is amplified by a 30 dB gain pre-amplifier, filtered with another narrow-band tunable OBPF, decoded by an asymmetric Mach-Zehnder delay interferometer (DLI) with 100-ps delay between the paths, detected by a balanced photodetector (BPD) and then sent into a bit-error-rate tester (BERT). The received power is monitored immediately at the 10% port of a 90/10 splitter for BER measurement.

To investigate the potential for chip-scale integration, a crystalline silicon (c-Si) waveguide is used as a FWM medium. The c-Si waveguide is fabricated using standard CMOS processes in a silicon-on-insulator (SOI) platform. The SOI wafer consists of 500 nm c-Si on top of 3 μm buried silicon dioxide (BOx). Thermal oxidation followed by hydrofluoric acid wet-etching of the oxide thins the top c-Si to 270 nm. Electron beam lithography and inductively coupled plasma (ICP) reactive ion etching are used to define the waveguide pattern. A thick (1 μm) silicon dioxide layer is deposited by plasma-enhance chemical vapor deposition (PECVD) for cladding and protection. The fabricated waveguide (270 nm by 600 nm) has low and anomalous group velocity dispersion, allowing for the wide-bandwidth FWM process [54,55]. The propagation loss of the c-Si waveguide is characterized by cut-back method to be ~3 dB/cm. Both ends of the waveguide have inversed taper

structures to improve the coupling efficiency [56]. Fiber-to-waveguide coupling is achieved through a lensed fiber and lens-collimator assembly.

3.4 Experimental Results

Modern optical communication systems are increasingly relying on advanced modulation formats to increase the information capacity of the lightwave carrier. To validate the modulation format transparency provided by our proposed wavelength multicasting scheme, both of a differential phase-shift keying (DPSK) and an on-off keying (OOK) demonstrations are presented here.

3.4.1 DPSK Demonstration

Figures 3.4(a)-3.4(c) show the optical spectra measured at the output of the optical comb source, HNLF, and silicon waveguide, respectively. As shown in Fig. 3.4(a), the uniformly-spaced spectral lines generated by the optical comb source are symmetric about the two CW seed laser sources with wavelength spacing of 0.4 nm. This wavelength spacing is chosen to correspond with the 50-GHz ITU grid. In both cases of the HNLF and the silicon waveguide, the wavelength of the signal wave carrying the testing 10-Gb/s DPSK data is λ_s = 1558.98 nm; the setup uses CW laser diodes set at λ_1 = 1549.6 and λ_2 = 1550 nm to seed the optical comb source. Using the pump waves from the optical comb source within a 5.3-nm wide window around 1550 nm, the HNLF and silicon waveguide output 26 and 15 multicast channels (including the channel at the input signal) transmitting DPSK data, respectively,

with sufficient power for error-free operation. In both cases, all of the uniformly-spaced multicast channels are distributed over both sides of the central pumps provided by the dual-seed optical comb source. As shown in Figs. 3.4(b) and 3.4(c), compared to the HNLF multicasting, the silicon waveguide solution possesses fewer error-free channels due to the coupling loss. The input and output coupling loss for the silicon waveguide is 13 dB and 8.1 dB, respectively. This can be improved by better design of the coupling taper and optimization of fabrication.

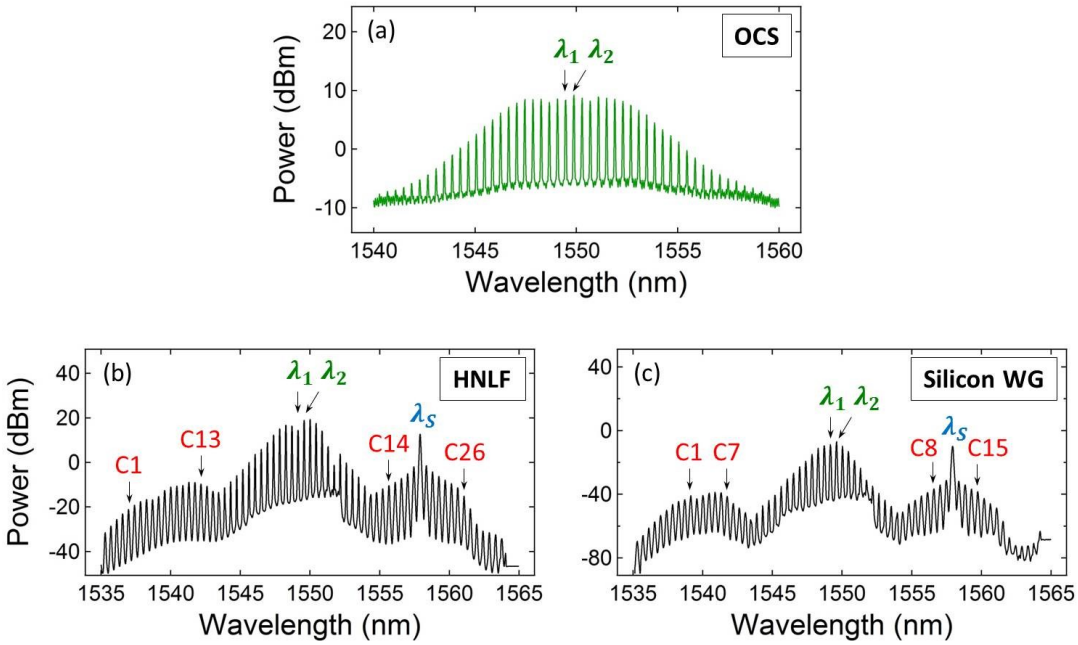

Fig. 3.4 (DPSK demonstration) Measured optical spectra immediately after (a) the OCS. The generated comb lines in the 5.3-nm wide window around 1550 nm are then isolated and used as pump sources to mix with a data-carrying signal for the multicasting experiment in (b) the 30-m long HNLF, and (c) the 15-mm long silicon waveguide. In both spectra of the HNLF and the silicon waveguide, multicast replicas are generated on both sides of the central comb pumps. Note: the wavelength spacing for all spectra is 0.4 nm. The resolution bandwidth of the optical spectra is 0.05 nm.

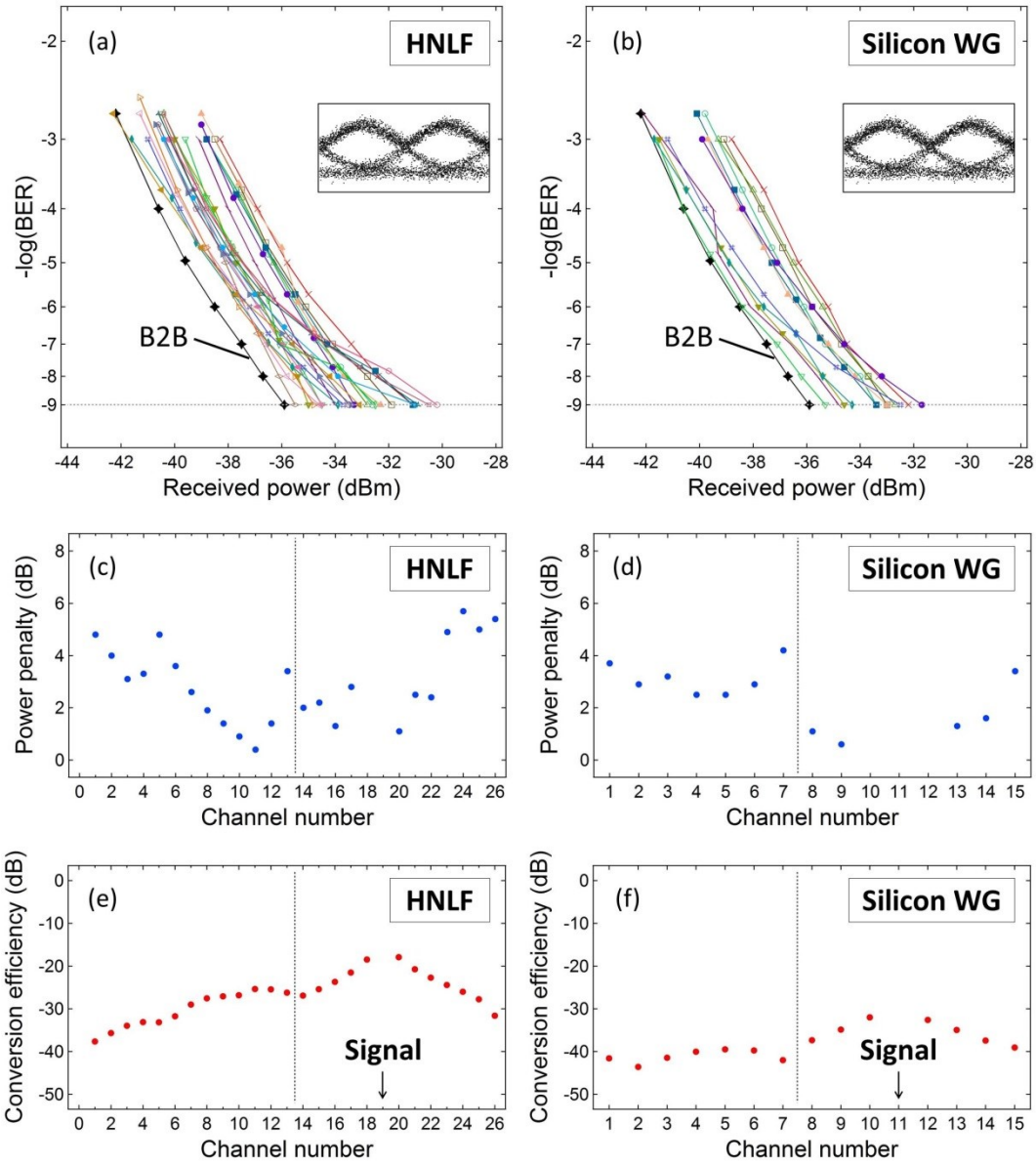

Fig. 3.5 (DPSK demonstration) BER validation, record of power penalty at BER = 10^{-9}, and conversion efficiency for the wavelength multicasting of 10-Gb/s DPSK data using (a), (c), (e) 30-m long HNLF, and (b), (d), (f) 15-mm long silicon waveguide. In (e) and (f), the input signal power is 52.5 mW for HNLF and 7.5 mW for silicon waveguide, respectively. Inset: eye diagram of the 10-Gb/s back-to-back DPSK data.

To illustrate the system performance, the BER of 10-Gb/s back-to-back (B2B) and multicast signals are shown in Figs. 3.5(a) and 3.5(b). Error-free (BER ≤ 10^{-9})

operation is acquired for all of the multicast channels in both the HNLF and silicon waveguide. For some multicast channels (C18, C19 for the HNLF, and C10-C12 for the silicon waveguide), the BER measurement is unavailable due to the lack of proper filters in this region where a strong signal is present; however, error-free operation is expected to be achieved since these channels possess adequate OSNR due to higher conversion efficiency. As shown in Figs. 3.5(c) and 3.5(d), HNLF achieves error-free operation with a maximum power penalty of 5.7 dB relative to the B2B measurement, while the silicon waveguide scheme acquires a maximum 4.2-dB power penalty in the worst performing channel. For both cases, the majority of channels possess a power penalty lower than 3 dB, and the center and edge channels with higher power penalties possess a reduced OSNR due to lower conversion efficiency. From Figs. 3.5(e) and 3.5(f), compared to the input signal power, the conversion efficiency of the error-free multicast copies ranges from -37.6 dB (C1) to -17.9 dB (C20) for the HNLF case, and from -43.6 dB (C2) to -32 dB (C10) for the silicon waveguide case, respectively. Here we define conversion efficiency as the ratio of the multicast channel power after the FWM interaction to the signal power at the start of the FWM interaction. Thus the propagation loss (4.5 dB) of the silicon waveguide is accounted for in the stated conversion efficiency. We note that our scheme achieves conversion efficiency comparable to that presented in [49,50] and that higher conversion efficiency can be expected with improved waveguide device design [57]. The relative conversion efficiency for each multicast channel is determined by both the power and phase of the pump comb lines that contribute to their generation. Therefore the equalization of the multicast channels can be

improved by adjusting either the relative power or phase of the comb lines. We note that it is preferable to control the flatness via the power profile of the comb lines. The ideal comb spectral phase is linear, which yields maximum conversion efficiency. Since the channels at the edge of the multicast spectrum are generated from fewer FWM pathways, we expect that a pump comb power profile with a flat center and more powerful lines towards the edges is ideal. However, we expect the primary equalization impairment in our experimental demonstration comes from the uncompensated (quadratic, cubic, etc.) spectral phase in the pump comb lines and this can be improved by better dispersion management of the pump comb source.

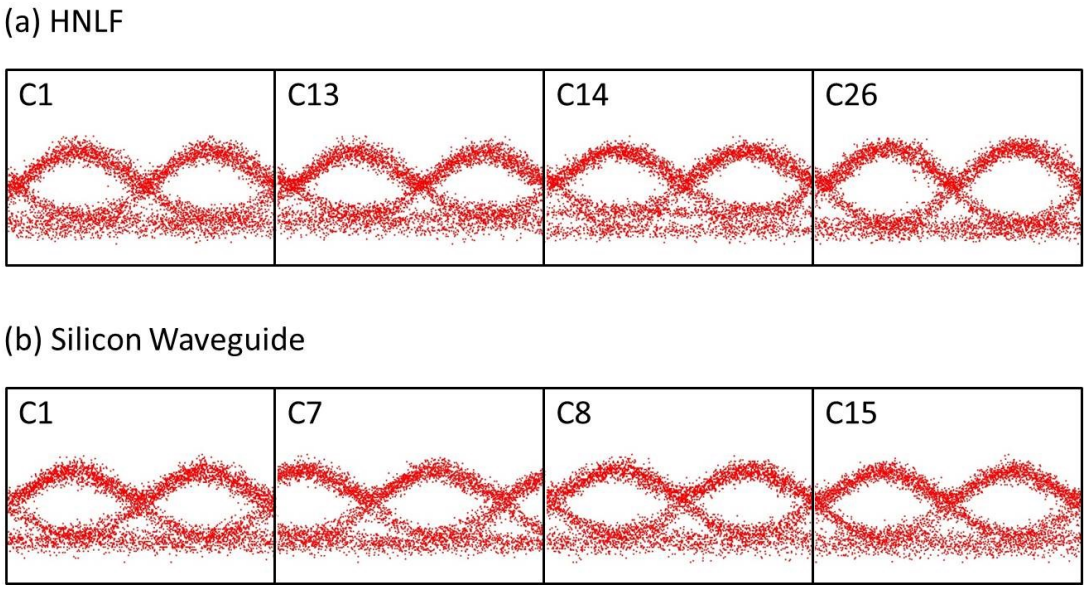

Fig. 3.6 (DPSK demonstration) Eye diagrams of 10-Gb/s DPSK data for select isolated multicast channels using (a) 30-m long HNLF and (b) 15-mm long silicon waveguide. All eye diagrams are taken at a BER of 10^{-9}.

Figure 3.6 shows the eye diagrams of some selected multicast channels carrying the DPSK data for both the HNLF and the silicon waveguide. For both nonlinear media, clear and open eye diagrams are achieved for all of the channels indicating that, as expected, this approach faithfully transfers the phase characteristics of the signal and allows for modulation format-transparent operation.

3.4.2 OOK Demonstration

The optical spectra measured at the output of the optical comb source, HNLF, and silicon waveguide are exhibited in Fig 3.7. The evenly-spaced spectral lines generated by the optical comb source are still symmetric about the two CW seed laser sources, but the wavelength spacing is now 0.8 nm (rather than 0.4 nm in the DPSK demonstration), as shown in Fig. 3.7(a). This wavelength spacing is chosen to correspond with the 100-GHz ITU grid. In all cases, the wavelength of the signal wave carrying the testing 10-Gb/s OOK data is λ_s = 1538.1 nm. For the case of the HNLF, the setup uses CW laser diodes set at λ_1 = 1549.4 and λ_2 = 1550.2 nm to seed the optical comb source. For the silicon waveguide demonstration, the seed CW lasers are shifted slightly to 1548.4 and 1549.2 nm. In both cases, the pump wavelengths are chosen to maximize the number of error-free multicast channels that are received. Using the six pump waves from the optical comb source, the HNLF and silicon waveguide output 23 and 14 multicast channels (including the channel at the input signal) transmitting OOK data, respectively, with sufficient power for error-free operation. In both cases, all of the evenly-spaced multicast channels are

still generated at both sides of the central comb source pumps. As presented in Figs. 3.7(b) and 3.7(c), in comparison with the HNLF scheme, the silicon waveguide solution possesses a spectrum with flatter response but fewer error-free channels due to the coupling loss. In OOK demonstration, the input and output coupling loss for the silicon waveguide is 13 dB and 6.6 dB, respectively. (In DPSK demonstration, the coupling loss at the input and output of the silicon waveguide is 13 dB and 8.1 dB, respectively.)

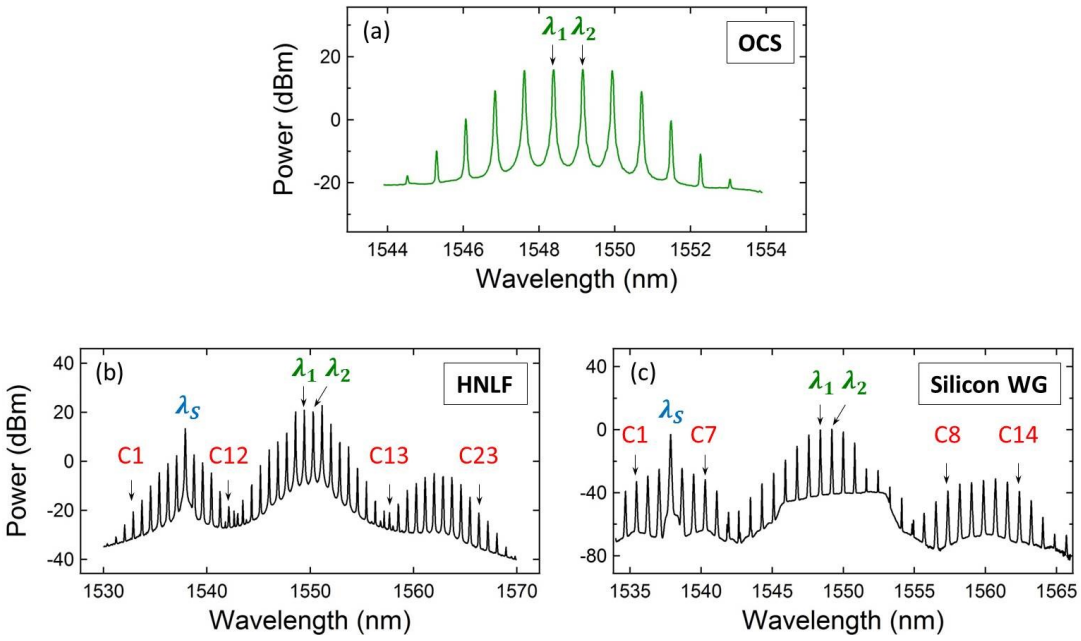

Fig. 3.7 (OOK demonstration) Measured optical spectra immediately after (a) the OCS. The highest six lines are then isolated and used as pump sources to mix with a data-carrying signal for the multicasting experiment in (b) the 30-m long HNLF, and (c) the 15-mm long silicon waveguide. In both spectra of the HNLF and the silicon waveguide, multicast replicas are generated on both sides of the central comb pumps. Note: the wavelength spacing for all spectra is 0.8 nm. The resolution bandwidth of the optical spectra is 0.05 nm.

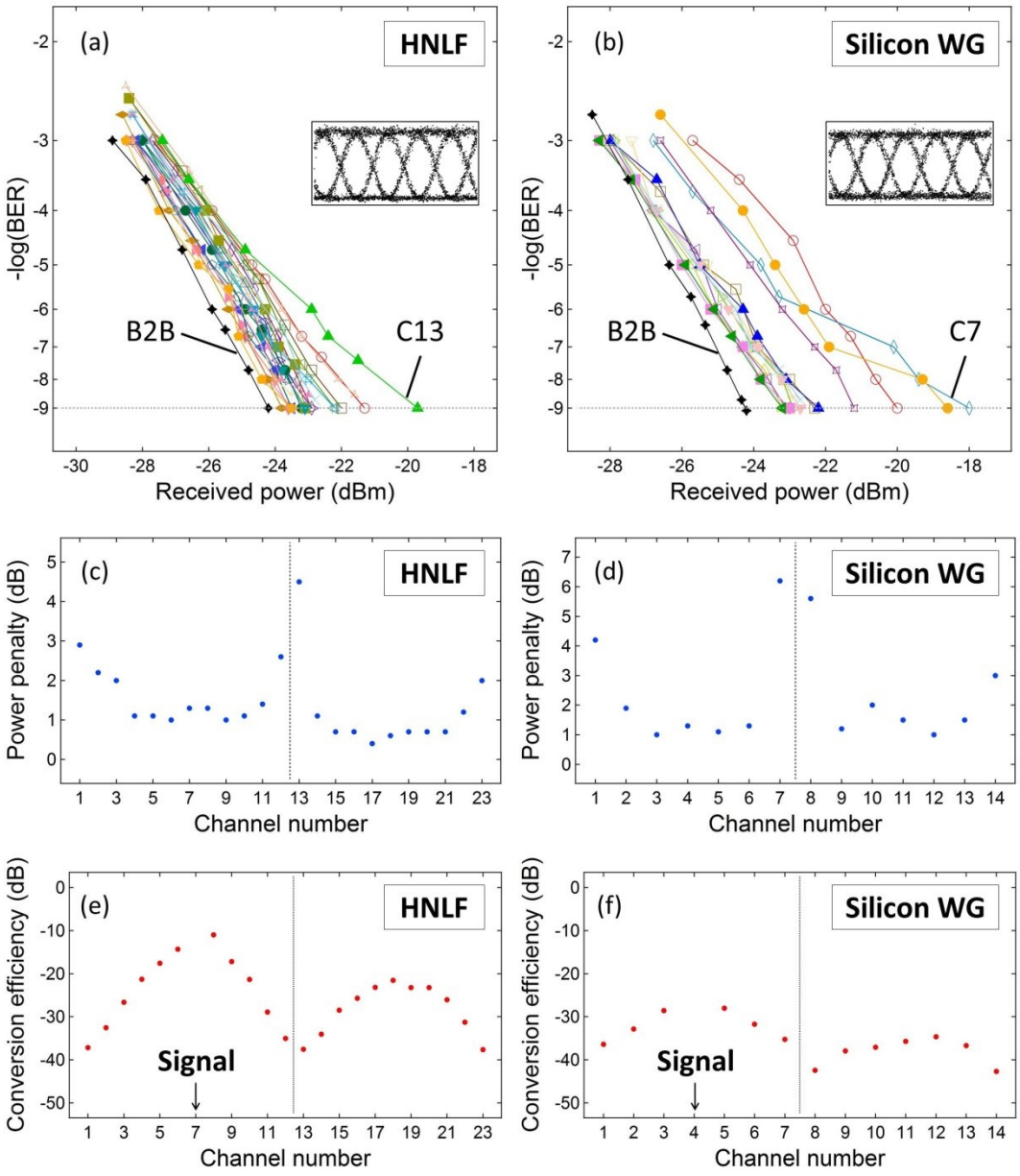

Fig. 3.8 (OOK demonstration) BER validation, record of power penalty, and conversion efficiency for the wavelength multicasting of 10-Gb/s OOK data using (a), (c), (e) 30-m long HNLF, and (b), (d), (f) 15-mm long silicon waveguide. In (e) and (f), the input signal power is 60 mW for HNLF and 10 mW for silicon waveguide, respectively. Inset: eye diagram of the 10-Gb/s back-to-back OOK data.

To clarify the operation performance, Figs. 3.8(a) and 3.8(b) show the BER of 10-Gb/s back-to-back (B2B) and multicast signals. For all of the multicast channels in

both the HNLF and silicon waveguide, the required error-free (BER ≤ 10^{-9}) reception is achieved. As shown in Figs. 3.8(c) and 3.8(d), HNLF achieves error-free operation with a maximum power penalty of 4.5 dB relative to the B2B measurement, while the silicon waveguide scheme acquires a maximum 6.2-dB power penalty in the worst performing channel. In this OOK demonstration, the majority of multicast channels possess a power penalty of ~1 dB for both nonlinear media, indicating that the FWM process in the HNLF and silicon waveguide are of equivalent quality from a communications perspective. The multicast channels at center and edge still possess higher power penalties and a degraded OSNR due to lower conversion efficiency. Furthermore, Figs. 3.8(c) and 3.8(d) also indicate that central channels have larger power penalties for similar signal strengths, this is likely due to the larger ASE and parametric fluorescence background noise for these center channels due to their proximity to the pumps. From Figs. 3.8(e) and 3.8(f), compared to the input signal power, the conversion efficiency of the error-free multicast copies ranges from -37.7 dB (C23) to -11 dB (C8) for the HNLF scheme, and from -42.7 dB (C14) to -28 dB (C5) for the silicon waveguide solution, respectively. Again, the conversion efficiency is defined as the ratio of the multicast channel power after the FWM interaction to the signal power at the start of the FWM interaction. Hence, the propagation loss (4.5 dB) of the silicon waveguide is accounted for in the stated conversion efficiency.

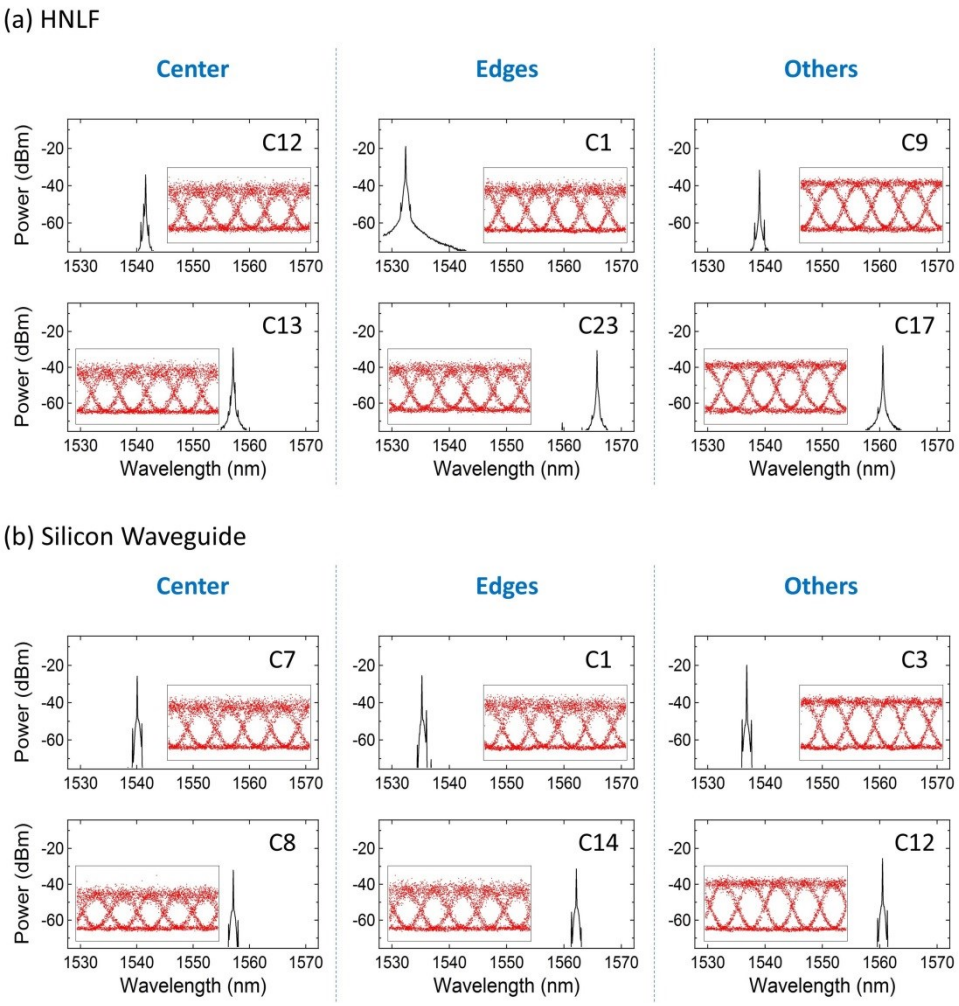

Fig. 3.9 (OOK demonstration) Optical spectra and eye diagrams of select isolated multicast channels carrying 10-Gb/s OOK data for (a) 30-m long HNLF and (b) 15-mm long silicon waveguide. For both media, the channels at the center and edges are slightly degraded while all other channels possess good quality. All eye diagrams are taken at a BER of 10^{-9}. The resolution bandwidth of the optical spectra is 0.05 nm.

Figure 3.9 shows the optical spectra and eye diagrams of some selected multicast channels for both HNLF and silicon waveguide. All channels exhibit open eye diagrams, while the non-central and non-edge channels (denoted "Others") have particularly clear and open eye diagrams.

3.5 Summary

An approach to wavelength multicasting with the aid of a dual-seed optical comb source is presented in this chapter. In this architecture, the dual-seed optical comb source is mixed with a data-carrying signal to undergo a cascaded four-wave mixing process (FWM) in a HNLF or a silicon waveguide, respectively. The evenly-spaced comb lines with a fixed phase relationship serve as both degenerate and non-degenerate FWM pumps, leading to a multitude of spectrally equidistant multicast idlers without noisy interference between the spectrally coincident FWM products. Furthermore, only two CW laser sources are used in the optical comb source representing a resource efficient and scalable approach to wavelength multicasting.

Our approach allows the phase information of the data-carrying signal to be preserved and replicated on all of the multicast channels, and therefore allows for format-transparent multicasting. To verify the modulation format transparency provided by the proposed scheme, both DPSK and OOK demonstrations using 10-Gb/s test data are carried out, respectively. In the DPSK demonstration, we obtain error-free (bit error rate, BER ≤ 10^{-9}) 26-way or 15-way wavelength multicasting in a highly-nonlinear fiber (HNLF) or a silicon waveguide, respectively. In the BER validation, error-free performance is achieved for all of the 26/15 channels with a typical power penalty of 3-dB in both nonlinear media. On the other hand, in the OOK demonstration, error-free 23-way and 14-way wavelength multicasting are achieved in a HNLF and a silicon waveguide, respectively. The majority of the 23/14 multicast channels possess a power penalty of ~ 1 dB.

Promisingly, the approach validated here provides a path towards full integration of the multicasting system on-chip through the incorporation of a chip-based comb source and hybridly integrated lasers and amplifiers [22,58], as illustrated in Fig. 3.10. Such a system is highly desirable for future WDM communications applications and ultrahigh-speed optical signal processing.

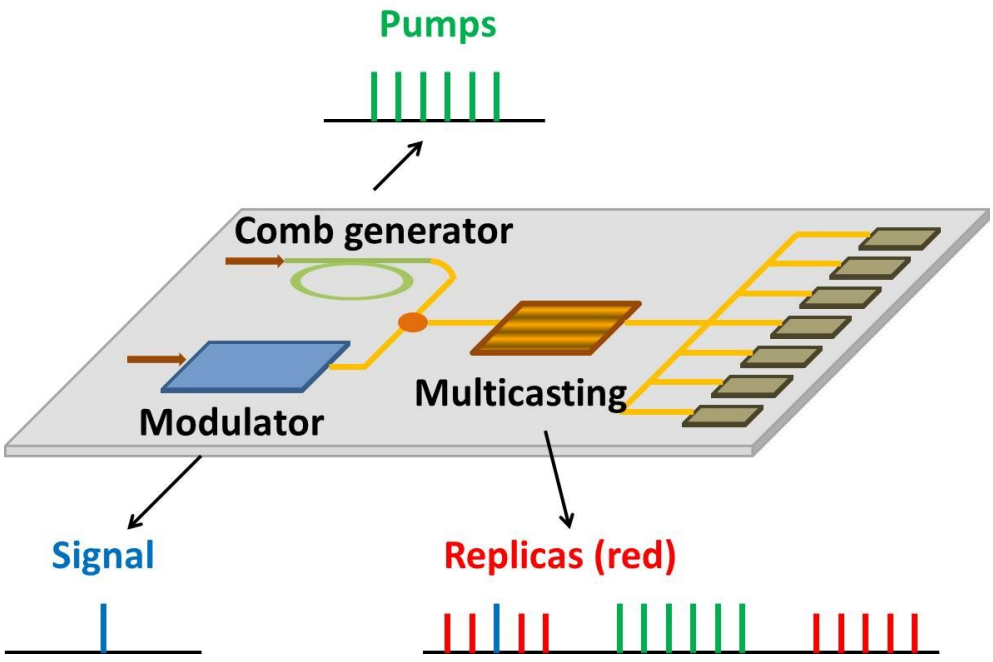

Fig. 3.10 An envisioned architecture of future on-chip wavelength multicasting.

Chapter 4

Photonic Analog to Digital Conversion

To store and process real world data in computers, an analog signal must be converted into a digital signal. An analog-to-digital converter (ADC) is used to give the digital representation of a real world signal, as shown in Fig. 4.1. The analog-to-digital conversion involves two processes including sampling and quantization. The sampling process is responsible for the conversion of a continuous-time signal into a discrete-time signal, while the quantization process turns continuous-amplitude values into discrete-amplitude patterns [59].

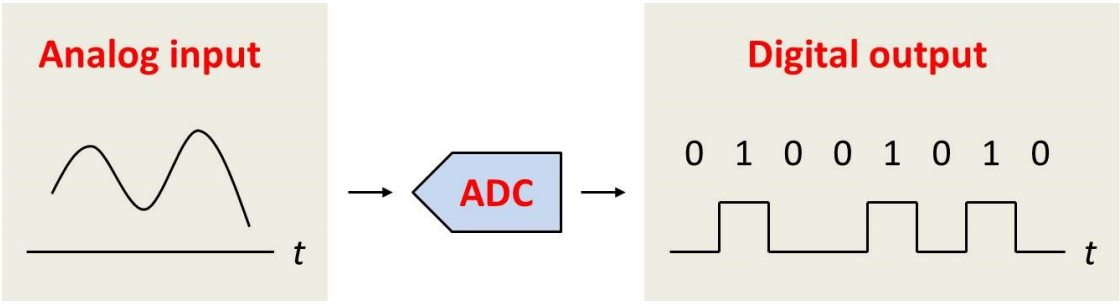

Fig. 4.1 The function of an analog-to-digital converter. An ADC is an interface system which converts an analog signal into a digital signal.

4.1 Introduction

As an interface component between analog and digital worlds, an analog-to-digital converter (ADC) used for conversion of an analog input into a digital output becomes indispensable due to the rapid evolution of digital signal processing. Consequently, the demand for digitization of a wideband signal makes this device essential to a variety of applications such as radar [60], sensor [61], and software-defined radio [62]. While most of the mature and practical solutions are carried out on electronic platforms, the advance of electro-optic technologies has led to major enhancements in speed and quality of ADCs. In particular, the features of broad bandwidth, low timing jitter, and high sampling rate offered by photonic ADCs have increasingly made these devices an desirable alternative to their electronic counterparts [63,64]. In addition to photonic assisted (time-stretch) [65,66] and photonic sampled [67,68] cases, various types of photonic ADCs with optical quantization have also been intensively investigated.

An early scheme proposed by Taylor utilized the folding characteristic in the transfer functions of an array of Mach-Zehnder modulators (MZMs) to achieve the optical quantization [69]. While this scheme was theoretically attractive, it imposed a major practical challenge by stringently requiring a set of MZMs with very low and geometrically scaled half-wave voltages, which brought difficulties in precise fabrication. In efforts to bypass such rigid requirements, other approaches to realizing the folding characteristics for optical quantization are demonstrated using cascaded MZMs [70] and a series of phase modulators (PMs) [71], respectively. In

spite of the successful demonstrations, these schemes are costly and possess limited scalability due to the need for multiple modulators. On the other hand, a solution to optical quantization based on a phase shift between the transfer functions of adjacent channels is first proposed by Stigwall and Galt [72,73]. In the scheme, the desired phase shift is introduced through the insertion of a single PM into one arm of a free-space Mach-Zehnder interferometer (MZI), and then an array of detectors and comparators at the output of the MZI are used to measure the fringe pattern and read out the signal in digitized form. Notably, this scheme removes the need for use of multiple modulators and initiates a variety of approaches to realizing ADCs with phase-shift optical quantization [74-78]. However, in most of this type of optical quantization architectures, a specific phase shift between channels is required and additional components or modules have to be implemented for applying and controlling the desired phase shift, bringing the complexity for system design. Importantly, the number of quantization levels is one of the basic parameters of ADCs. Assume the number of code bits or channels is N, the maximal number of quantization levels is 2^N for folding-type quantization [69-71], while this quantity is limited to be $2N$ for shifting-type quantization due to the use of circular codes [72-78]. Furthermore, differential encoding benefits the resolution of ADC systems since a differential-encoding digitized signal is expected to possess reduced quantization noise compared to a direct-encoding digitized signal with the same number of bits [77,78].

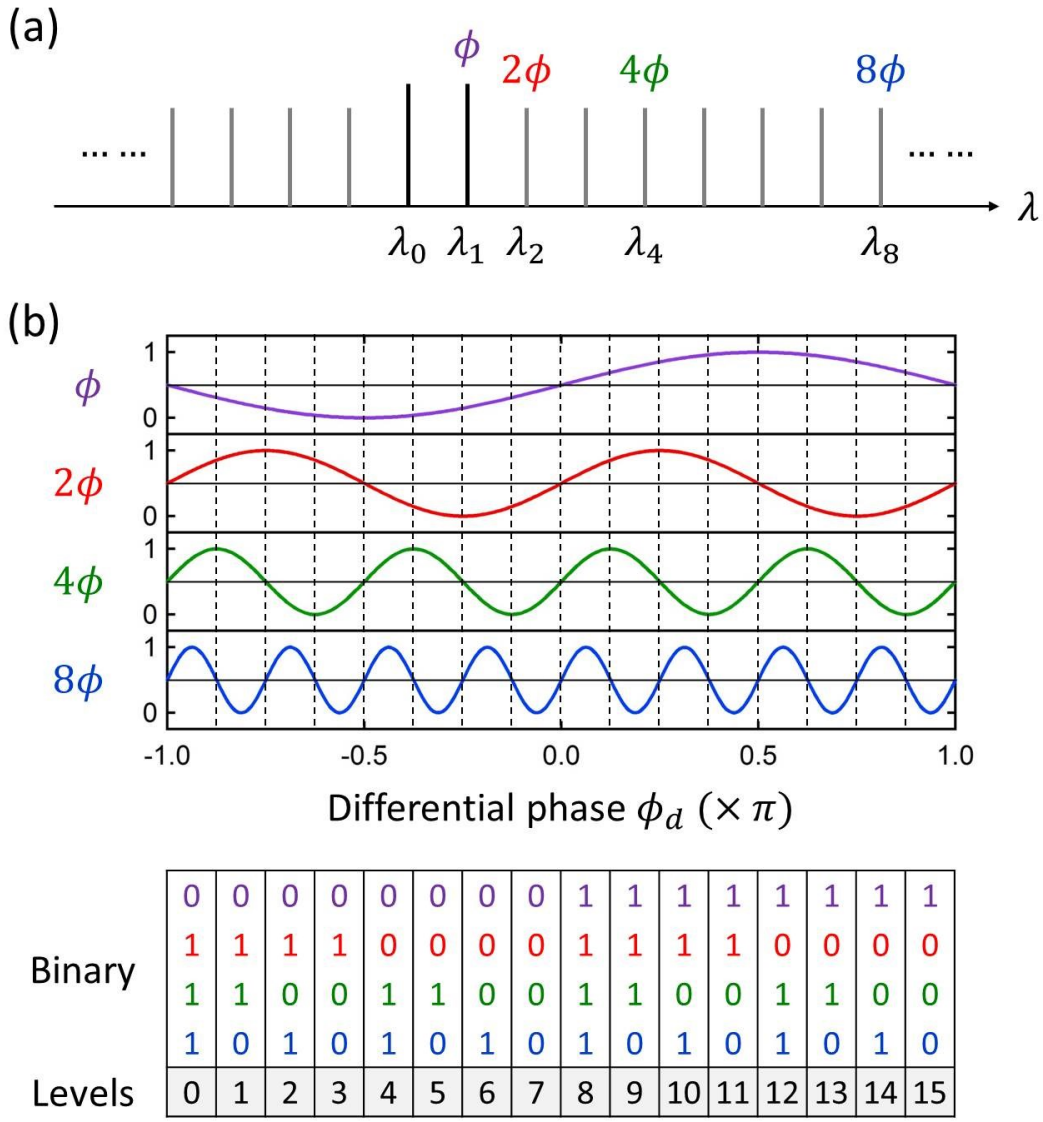

Binary	0	0	0	0	0	0	0	0	1	1	1	1	1	1	1	1
	1	1	1	1	0	0	0	0	1	1	1	1	0	0	0	0
	1	1	0	0	1	1	0	0	1	1	0	0	1	1	0	0
	1	0	1	0	1	0	1	0	1	0	1	0	1	0	1	0
Levels	0	1	2	3	4	5	6	7	8	9	10	11	12	13	14	15

Fig. 4.2 Principle of operation. (a) By mixing a seed at λ_0 with another signal-carrying seed at λ_1 to induce a parametric process, a dual-seed optical comb source provides desired phase harmonics. (b) Transmission responses of a MZI are sinusoidal functions of differential phase. From the transfer functions of four channels, binary sequences and corresponding quantization levels are determined.

4.2 Principle

Figure 4.2 illustrates the principle of operation of the optical quantization and differential encoding used in our proposed ADC architecture. First, as depicted in Fig. 4.2(a), by mixing a continuous-wave (CW) pump laser at wavelength λ_0 with a phase-modulated signal $\phi(t)$ at λ_1 to seed a cascaded FWM comb source in a nonlinear medium, a series of phase harmonics of the signal can be created through the phase transfer of parametric processes [79]. Four comb lines at λ_k with phases $k\phi(t)$, where k = 1, 2, 4 and 8, are isolated and then sent into an asymmetric MZI with a delay τ between its two arms. For each component at λ_k, we can define its corresponding differential phase at the output of the MZI as $k\phi(t) - k\phi(t - \tau) = k\phi_d(t)$, where $\phi_d(t) = \phi(t) - \phi(t - \tau)$ is the differential phase of the input signal at the output of MZI. The response of a MZI is a sinusoidal function of differential phase ϕ_d since the photocurrent I_k generated by a photodetector in an interferometric detection is proportional to $\sin(k\phi_d)$ at quadrature operation for each component λ_k [80], as shown in Fig. 4.2(b). Therefore, the folding transfer functions can be generated due to the phase harmonics provided by the dual-seed optical comb source. Following, a threshold is set to be at the middle of full scale to determine the binary values of 1 or 0 in each channel. The differential encoding is accomplished by assigning a corresponding level to each binary sequence in order (see Fig. 4.2(b)). Note that the signal to be quantized and encoded here is the input differential phase $\phi_d(t)$ instead of the original phase $\phi(t)$ [77,78].

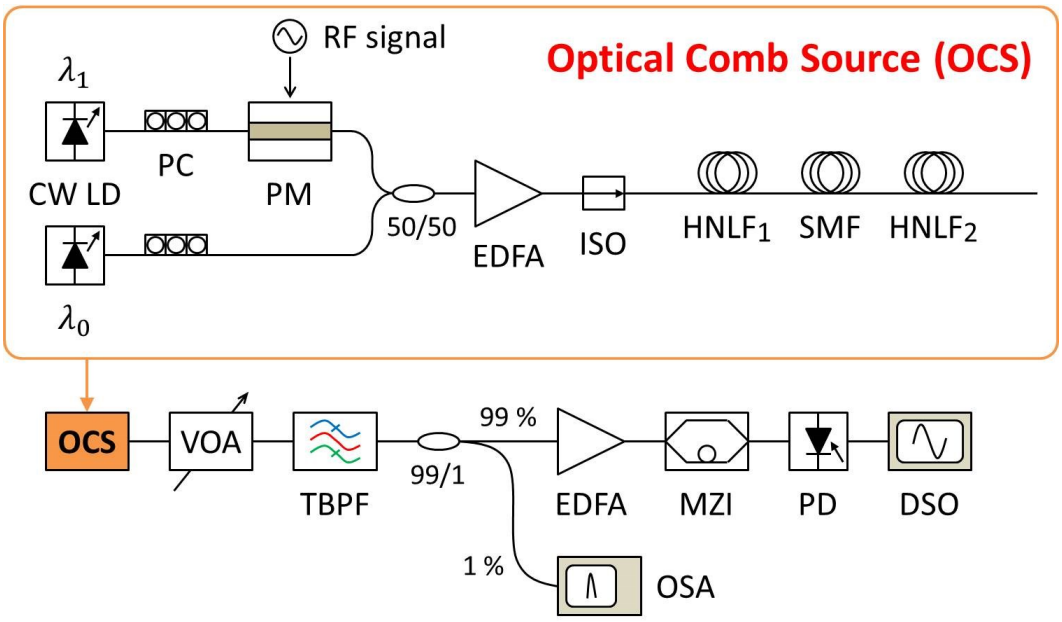

Fig. 4.3 Experimental setup. CW LD: continuous-wave laser diode, PC: polarization controller, PM: phase modulator, EDFA: erbium-doped fiber amplifier, ISO: optical isolator, HNLF: highly-nonlinear fiber, SMF: single-mode fiber, VOA: variable optical attenuator, TBPF: tunable band-pass filter, MZI: Mach-Zehnder interferometer, PD: photodetector, DSO: digital sampling oscilloscope, and OSA: optical spectrum analyzer.

4.3 Experimental Setup

Figure 4.3 depicts the architecture of our proposed ADC system in which a dual-seed optical comb source can produce a sequence of comb components with phase harmonics. In the optical comb source [26,27], two CW laser diodes (New Focus, 6700 series, TLB-6728-P) at λ_0 and λ_1 followed by polarization controllers (PCs) are used as seeds, one of which at λ_1 carries an analog radio-frequency (RF) signal through a 20-GHz PM (EOSPACE, PM-0K5-20-PFU-PFU, the half-wave voltage V_π is 5.9 V). The two waves with one phase-modulated are combined by a 3-dB coupler, amplified by an erbium-doped fiber amplifier (EDFA), and injected into two

cascaded spans of highly-nonlinear fiber (HNLFs) separated by a tailored length of single-mode fiber (SMF). The lengths of two sections of HNLFs (OFS, with nonlinear coefficient of 11.5 $W^{-1}km^{-1}$, and zero dispersion wavelength is around 1550 nm) used as FWM stages are 88 and 100 m, and the SMF which serves as a compressor is 400-m long. To suppress the stimulated Brillouin scattering (SBS) and hence increase the mixer bandwidth, a 10-step stair-ramp strain plan is longitudinally applied to the first stage of HNLF [27-30].

Next, the entire output of the optical comb source is attenuated by a variable optical attenuator (VOA) and sent into an optical tunable band-pass filter (TBPF) to individually isolate each channel with the desired phase harmonics. For each isolated channel, in addition to 1% tapped off for monitoring, the rest is amplified by a pre-EDFA and launched into an asymmetric MZI with 100 ps of delay between its two arms to generate a corresponding differential phase signal. The signal is then detected and converted into an electrical signal by a 45-GHz photodetector (PD, Discovery Semiconductors, DSC 10H) so that the temporal waveforms for each channel can be captured by a digital sampling oscilloscope (DSO, Tektronix, 11801C). Once the recorded traces of the four channels with desired phase harmonics are collected, these waveforms are sampled at a fixed rate by a software program which plays the role of a pulse train [74,81]. Finally, by comparing the sampled data with threshold, a sequence of binary values and corresponding levels are obtained for quantization, and therefore the functionality of digitization is achieved.

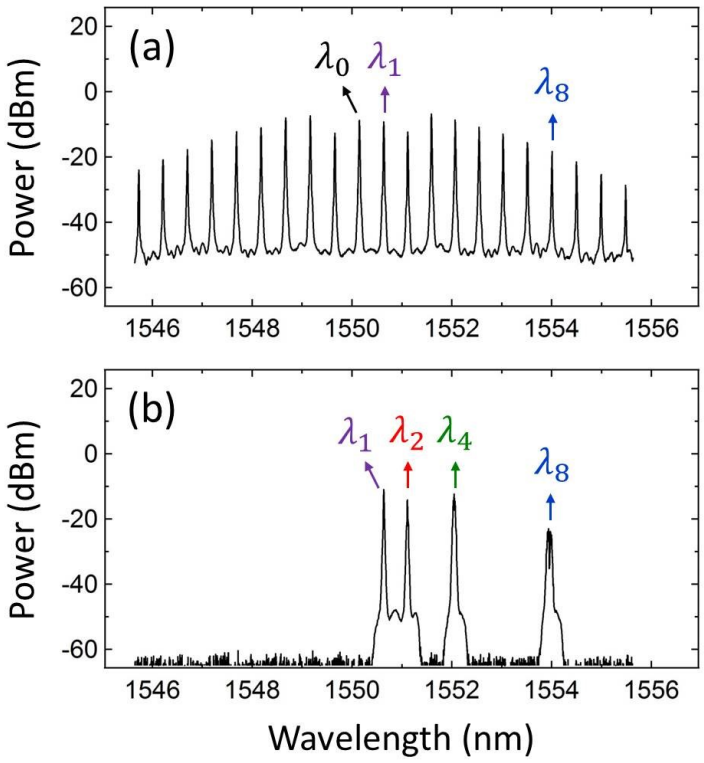

Fig. 4.4 Measured optical spectra of the optical comb source when (a) signal is absent and TBPF is off, and (b) signal is present and TBPF is on. The resolution bandwidth of both optical spectra is 0.01 nm.

4.4 Experimental Results

To implement the optical comb source, the two CW seed lasers output 17 and 20 mW at λ_0 = 1550.16 nm and λ_1 = 1550.64 nm, respectively, and the EDFA operates at 1.6 W. Figure 4.4(a) shows the optical spectrum of the optical comb source measured by an optical spectrum analyzer (OSA) at the 1% tap when an RF signal is absent and the TBPF is transparent. Measured power at the output of optical comb source and VOA are 480 and 55 mW, respectively. The required higher-order harmonics are generated at λ_2 = 1551.12, λ_4 = 1552.08, and λ_8 = 1554 nm when an

RF signal is applied through the PM, as seen in Fig. 4.4(b). For each one-channel measurement, the bandwidth of optical TBPF is set to be 50 GHz for individually isolating a single comb component at λ_k (k = 1, 2, 4, and 8).

To demonstrate the basic functionality of digitization supported by the proposed architecture, a signal generator (HP, 8341B Synthesized Sweeper) provides a single tone of 2.44 GHz sinusoidal signal, $V(t)$ or $\phi(t) = (\pi/V_\pi)V(t)$, which is first amplified to 18 dBm and then added to the link through the PM in the optical comb source. Due to the parametric generation by the optical comb source, each generated wave λ_k (k = 1, 2, 4, and 8) carries a multiple of the input signal, $kV(t)$ or $k\phi(t)$. In each individual one-channel measurement, only one of the desired four comb components is isolated by a TBPF and amplified to around 10 mW by a pre-EDFA. This selected component with desired phase harmonic is then launched into an asymmetric MZI with delay τ = 100 ps, and therefore its corresponding differential signal $kV_d(t) = kV(t) - kV(t - \tau)$ or $k\phi_d(t) = k(\pi/V_\pi)V_d(t)$ can be obtained at the output of MZI. Following, the differential signal is detected by a 45-GHz photodetector and the temporal waveform is captured by a DSO, as shown in Fig. 4.5(a). The fundamental pitch at λ_1 in well agreement with simulation result (dashed curve) corresponds to the most significant bit (MSB), while the highest-order harmonic at λ_8 which represents the least significant bit (LSB) possesses a relatively complicated waveform. The recorded four traces are sampled at a uniform rate by a software program, and various sets of binary values collected from the four channels at every sampling point and their corresponding quantization levels can be acquired by comparing each sampled waveform with an adjustable threshold set to

be around the middle of full scale. Here, the threshold values of the four channels are slightly different for reducing errors. As can be seen from Fig. 4.5(b), the digitization with eight quantized levels for a sinusoidal signal is achieved (orange dot). A sinusoidal reference (dashed curve) is also shown in Fig. 4.5(b) for comparison, and a small amount of errors are present due to the deviation of the detected waveform of the highest-order harmonic.

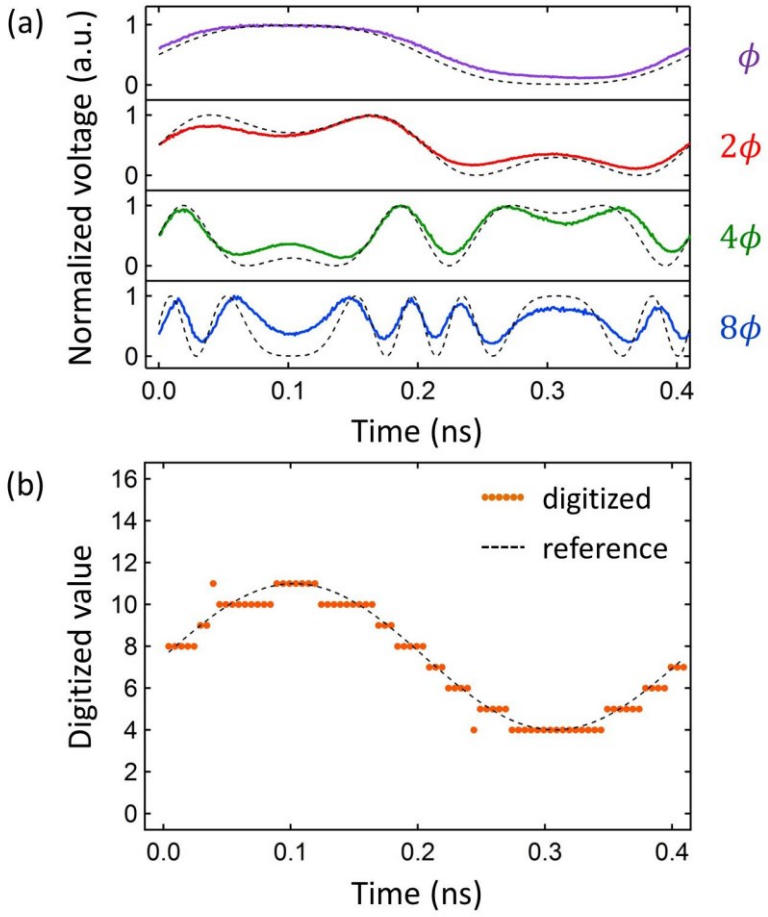

Fig. 4.5 Digitization of a single tone of sinusoidal signal. (a) Recorded temporal waveforms (solid) and theoretical traces (dashed) for four channels. (b) Digitized signal (orange) and reference (dashed).

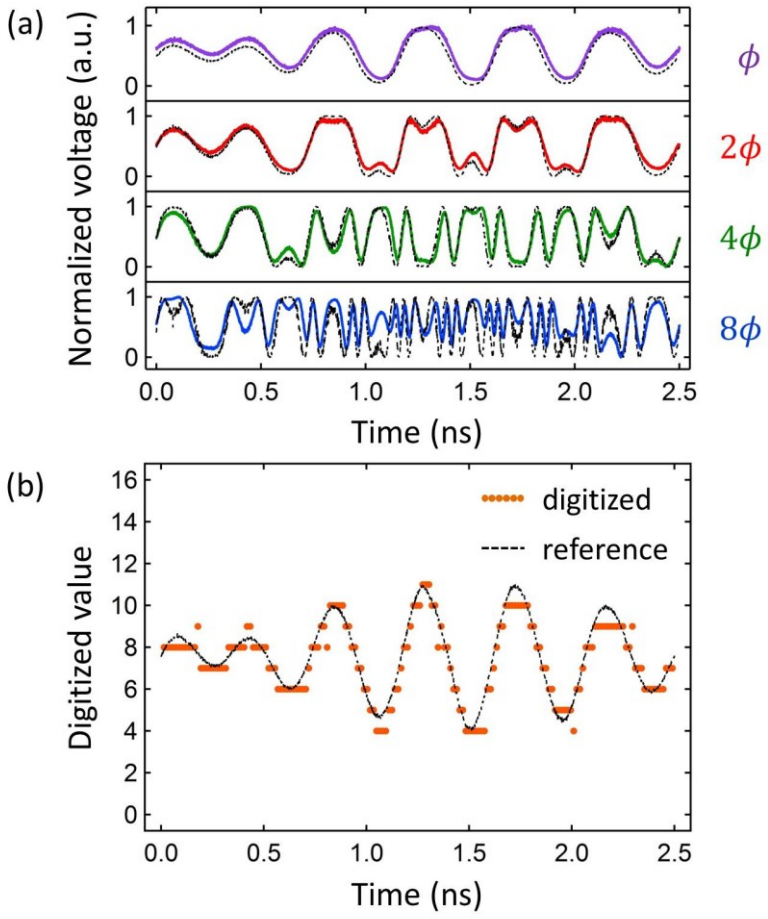

Fig. 4.6 Digitization of a sophisticated signal. (a) Recorded temporal waveforms (solid) and theoretical traces (dashed) for four channels. (b) Digitized signal (orange) and reference (dashed).

The proposed architecture is capable of digitizing an electrical signal with a complicated waveform. As an example, a target signal is first generated by mixing a 2-GHz sinusoidal signal with another 2.5-GHz sinusoidal signal. The same PM, optical comb source, and asymmetric MZI are still utilized to create the desired harmonics and their corresponding differential signals. Figure 4.6(a) presents the measured traces (solid curves) and simulation results (dashed curves), respectively, for the four channels. While all the four temporal waveforms become complex in

this example case due to the sophisticated signal, the recorded traces of the first three channels are still in well agreement with theory. The last channel varies with time rapidly since the highest-order harmonic corresponds to a severe phase modulation. According to the measured traces, a digitized signal with eight quantized levels is obtained, as shown in Fig. 4.6(b). Compare with the reference (dashed curve), the main source of errors is the misjudgment of the LSB, representing the need for correction of the highest-order harmonic. It is expected to improve by fine tuning the wavelength of one laser diode used in the optical comb source for quadrature operation.

For the above both example cases of simple and sophisticated input signals, the minimum and maximum quantized levels are 4 and 11, which are equivalent to differential phases of $-\pi/2$ and $\pi/2$, respectively. The full range of differential phase that can span is determined by the input RF power of the original signal. Therefore, in both of our 4-bit demonstrations, it is expected to increase the number of quantization levels to $2^4 = 16$ if the RF power for the input signal can be further enhanced. On the other hand, the primary factor which results in errors in the proposed scheme is the severe modulation of highest-order harmonic, and the degradation due to this can be alleviated by fine tuning the wavelength of the seed lasers to satisfy the requirement for the quadrature operation and/or by properly adjusting the comparator threshold to guarantee correct binary decisions near crossings.

4.5 Summary

In summary, we experimentally demonstrate an ADC scheme with optical quantization and differential encoding utilizing a dual-seed optical comb source and an asymmetric MZI. The use of 4 phase harmonics provided by the optical comb source, which removes the need for multiple modulators, enables the generation of period-folding transfer functions and hence greatly simplifies the system design. Promisingly, the proposed ADC architecture possesses potential for on-chip integration, and such a system is attractive to future signal processing facilities. As a proof of concept, the digitization with a quantization level of 8 for both a simple and a sophisticated analog signal is achieved, validating the feasibility of our proposed scheme.

Chapter 5

Photonic Microwave Delay-Line Filters

(Future Work)

In addition to the wavelength multicasting (Chapter 3) and the photonic analog-to-digital conversion (Chapter 4), the dual-seed optical comb sources discussed in this work also can find applications in microwave photonic signal processing. Importantly, a photonic microwave delay-line filter with complex coefficients is one of the indispensable devices in microwave photonic signal processing. In this chapter, the first section is devoted to the discussion on the architectures of practical photonic microwave delay-line filters. A brief simulation on characteristics of this filter is presented in the second section. To verify the feasibility of incorporation of dual-seed optical comb sources into the design of photonic microwave delay-line filters, the preliminary experimental results are given in the third section. The last section summarizes the main conclusions of the entire study.

5.1 Architectures

In microwave photonic (MWP) signal processing, a key device is a photonic microwave delay-line filter. To implement such type of filters, a primary building block is a tapped delay line which provides multiple weighted and delayed taps. The concept of tapped delay lines [40] is illustrated in Fig. 5.1. Each tap in the N-tap delay line extracts the input signal $x(t)$ at different time intervals T_k, and the delayed signal in each tributary is scaled by a corresponding (complex) coefficient a_k and then summed with other copies in different taps to create an output signal $y(t)$. Therefore, the output signal from a tapped delay line can be expressed as

$$y(t) = \sum_{k=0}^{N-1} a_k x(t - T_k) = \sum_{k=0}^{N-1} a_k x(t - kT) \tag{5.1}$$

where T_k is the time delay for the k-th tap, T is the time delay difference between consecutive taps, and $T_k = kT$, $k = 0, 1, 2, ..., N\text{-}1$.

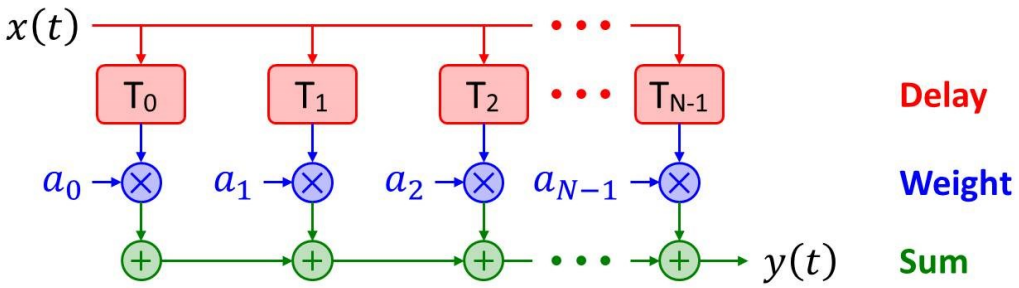

Fig. 5.1 The concept of a tapped delay line. An input signal is tapped at various time delays, each tributary is scaled, and then all taps are added.

A conventional scheme of a photonic microwave delay-line filter [82] generally consists of a single optical source, a modulator, multiple delay-line components, and a photodetector, as shown in Fig. 5.2. An optical carrier is injected into an electro-optic modulator (EOM) driven by a radio-frequency (RF) signal, and then the RF-modulated optical carrier is split into N tributaries. The weight of each tap can be adjusted by inserting an individual amplifier or attenuator. Importantly, the RF-modulated optical signal in the kth tap (k = 0, 1, 2, ..., N-1) experiences an accordingly time delay, kT, where T is the time-delay difference between successive taps. After being combined by a coupler, these weighted and delayed signals are sent into a photodetector. This scheme is straightforward; however, the tunability is limited by requiring a replacement of multiple delay lines to obtain the desirable time-delay difference.

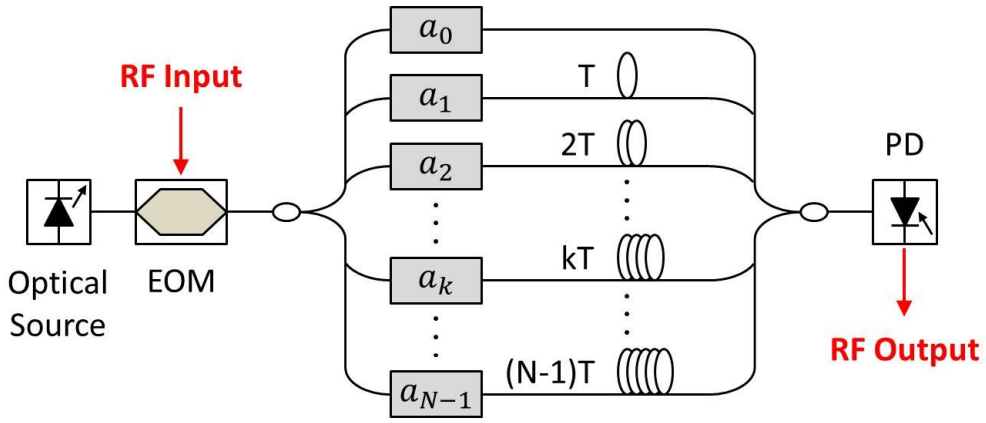

Fig. 5.2 A conventional scheme of a photonic microwave delay-line filter. The required time delays for all taps are achieved by means of individual optical fibers with tailored length.

An alternative solution [83,84] using either multiple individual optical sources (e.g., an array of lasers) or a multi-wavelength optical source (e.g., optical comb

source) possesses the desirable tunability. In the scheme, multiple optical carriers and a single dispersive delay line are utilized, as presented in Fig. 5.3. The weight of different taps can be tuned by separately changing the optical power at different wavelengths (not shown in the figure), and the time-delay difference between consecutive taps is adjusted by varying the wavelength spacing among the optical carriers. If the multi-wavelength source produces spectral components with wavelength spacing $\Delta\lambda$, the time-delay difference is determined by $T = DL\Delta\lambda$, where D is the dispersion parameter of the dispersive component and L is its length. With the combination of an efficient multi-wavelength source and a dispersive device, this architecture can greatly simplify the system and readily provide the tunability.

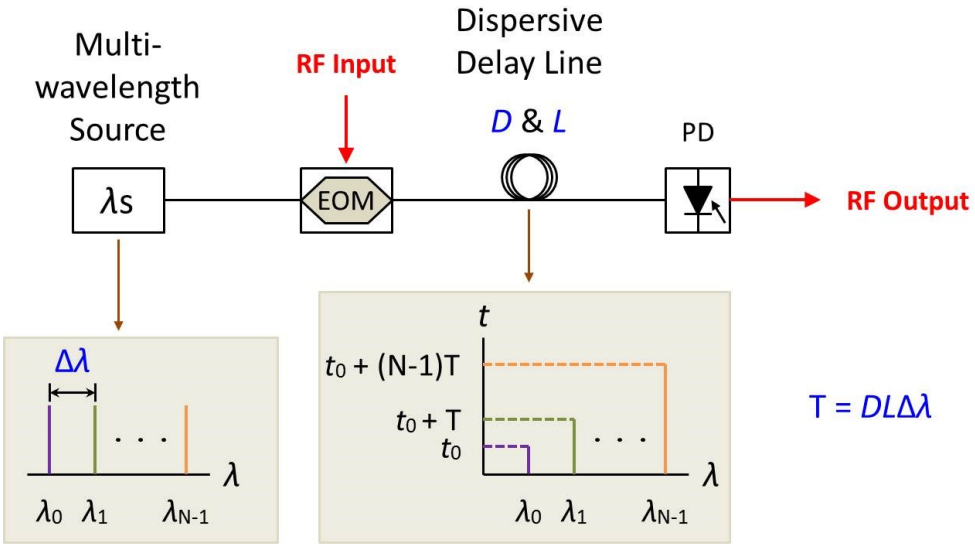

Fig. 5.3 An alternative scheme of a photonic microwave delay-line filter. The time-delay difference is tunable by using a combination of a multi-wavelength source and a single dispersive component. Once the dispersive component is given, the time-delay difference is determined by the wavelength spacing between successive spectral lines of the multi-wavelength source.

Here, the dual-seed optical comb source can provide the optical carriers. If the dispersive element is given, the required time-delay difference is achieved by tuning the wavelength separation of the two seed lasers in the comb source setup. Consequently, the dual-seed optical comb source is a suitable candidate for the photonic microwave delay-line filters due to the flexibility of comb spacing.

5.2 Simulations

Majority of the demonstrated architectures operate under the incoherent regime to be immune from optical interference and hence are subject to all-positive tap coefficients which correspond to optical intensities, but this limitation causes such photonic microwave filters to be only used as low-pass filters [82,85]. On the other hand, various schemes of photonic microwave delay-line filters with complex tap coefficients have been continually proposed to realize the implementation of a bandpass filter [86-90].

The transfer function of an *N*-tap delay-line filter with complex coefficients can be expressed as [82,85]

$$H(f) = \sum_{k=0}^{N-1} a_k e^{-j2\pi fkT} = \sum_{k=0}^{N-1} |a_k| e^{jk\theta} e^{-j2\pi fkT} \tag{5.2}$$

Where f is the RF frequency, a_k is the complex coefficient of the kth tap, θ is the phase shift between consecutive taps, and T denotes the time-delay difference. From the above equation, the transfer function of the filter possesses a periodic

characteristic, and the period in the frequency domain is referred as the free spectral range (FSR) which is the reciprocal of the time-delay difference between adjacent taps. Furthermore, the photonic microwave delay-line filters can be tuned by varying the number of taps (N), time-delay difference (T), and the complex coefficients (a_k) including magnitude and phase shift (θ).

Basically, the dual-seed optical comb source can provide a multitude of optical carriers for implementing the required number of taps. Following, for simplicity, consider a 4-tap photonic microwave delay-line filter in our simulations. Here, the magnitude of complex coefficients for the four taps is set to be identical. If a spool of standard single-mode fiber with a dispersion parameter D = 17 ps/nm/km and length L = 5000 m is used as the dispersive element, the product DL = 85 ps/nm is fixed in the simulation example. Note that the time-delay difference is given by $T = DL\Delta\lambda$ and the free spectral range FSR = $1/T$.

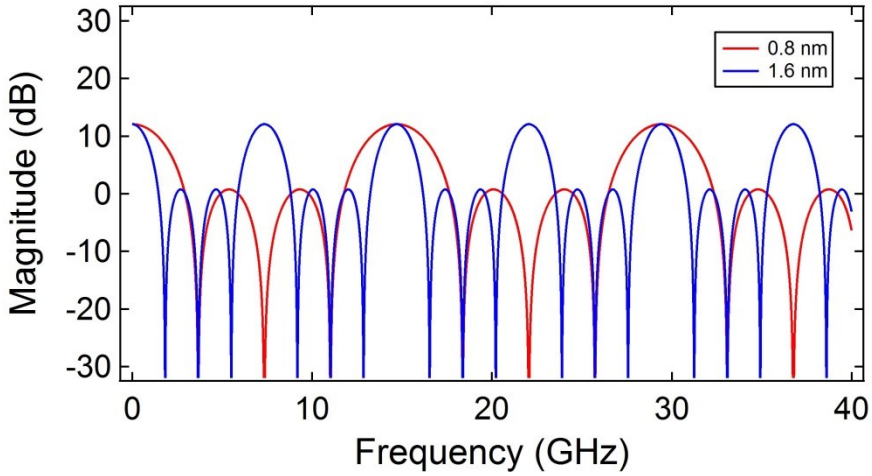

Fig. 5.4 The first set of simulation examples. The wavelength spacing between consecutive spectral lines in the multi-wavelength source is 0.8 nm (red) and 1.6 nm (blue), respectively.

Figure 5.4 shows the results of the first set of the simulation. Two optical comb sources with spectral spacing of 0.8 and 1.6 nm are utilized. The former ($\Delta\lambda$ = 0.8 nm) causes a time-delay difference T = 68 ps and a free spectral range FSR = 14.7 GHz (red curve), while the latter ($\Delta\lambda$ = 1.6 nm) corresponds to T = 136 ps and FSR = 7.35 GHz (blue curve). This simulation example indicates the free spectral range of the filter can be tuned by adjusting the comb spacing, and this parameter in the dual-seed optical comb source is determined by the wavelength separation of the two seed laser sources.

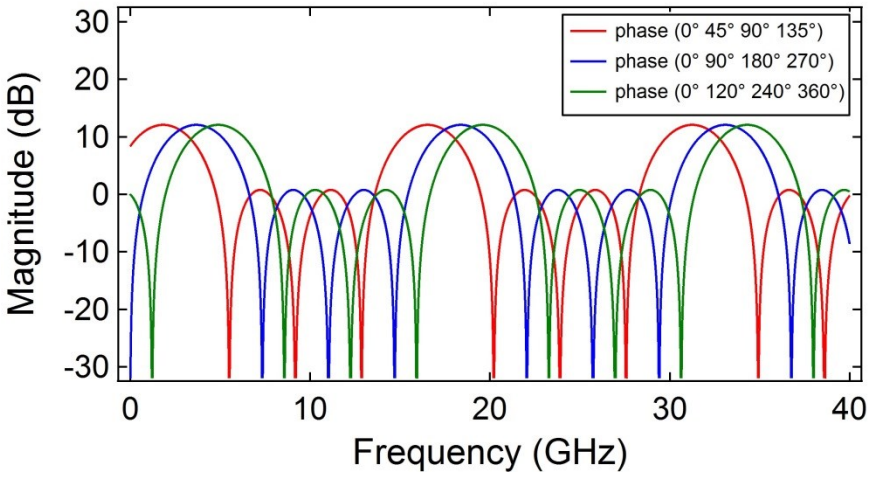

Fig. 5.5 The second set of simulation examples. For all of the three cases in this set, the wavelength spacing between adjacent spectral lines in the multi-wavelength source is fixed at 0.8 nm. These three cases possess different arrangement of phase shifts for four taps (see legend).

In the second set of the simulation, a comb source with $\Delta\lambda$ = 0.8 nm is applied to three cases which have different arrangement of phase shifts. The three example cases share an identical time-delay difference T = 68 ps and FSR = 14.7 GHz. The phase shifts for the four taps in these three cases are (0°, 45°, 90°, 135°) for the first

case, (0°, 90°, 180°, 270°) for the second case, and (0°, 120°, 240°, 360°) for the last case. As shown in Fig. 5.5, for the three cases, the central frequency of the filters is shifted, while the free spectral range, 3-dB bandwidth, and the main to secondary sidelobe ratio (MSSR) are identical. Therefore, the tunability of central frequency can be realized by giving proper phase shifts to the taps.

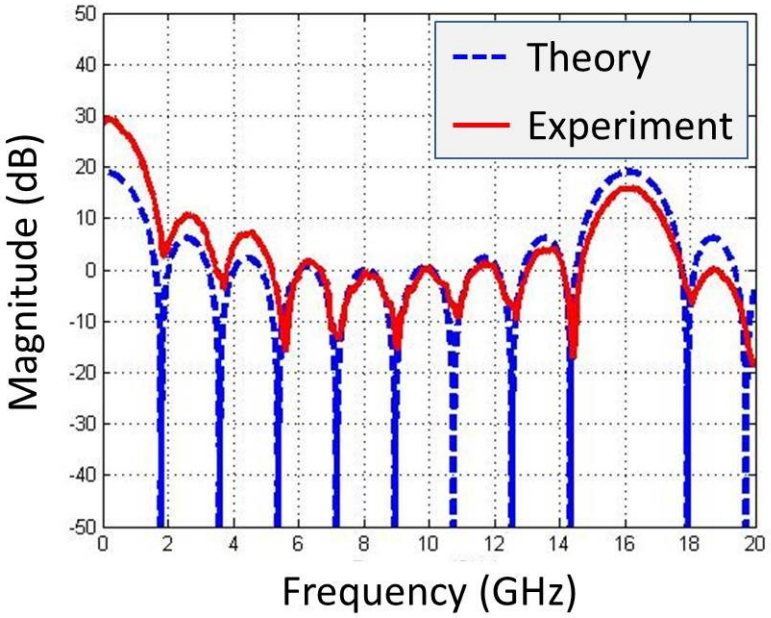

Fig. 5.6 The preliminary experimental result. A 9-tap photonic microwave delay-line filter is achieved. The wavelength spacing between successive spectral components in the dual-seed optical comb source is 0.8 nm, and each tap possesses an identical weight. The blue dash curve: theory, and the red solid curve: experimental result.

5.3 Preliminary Experimental Results

Figure 5.6 shows the preliminary experimental result. The dispersive element used here is a 4560-m long single-mode fiber with dispersion parameter D = 17

ps/nm/km, and thus the product DL = 77.5 ps/nm. The wavelength separation between two seed laser sources in the dual-seed optical comb source is $\Delta\lambda$ = 0.8 nm. Therefore, the time-delay difference T = 62 ps, and the free spectral range FSR = 16.1 GHz. In the figure, the blue dash curve represents the theoretical result and the red solid curve shows the experimental result. Here, a 9-tap photonic microwave delay-line filter can be obtained, and each tap has identical weight.

Recent research on photonic microwave delay-line filters with complex coefficients has drawn much attention due to the practical functionality for microwave photonic signal processing. It is promising to incorporate the aforementioned dual-seed optical comb sources into the design and implementation of photonic microwave delay-line filters since the desirable tunability and reconfigurability can be enabled by comb sources. In the future, it is expected to increase the number of taps and investigate the filter features including 3-dB bandwidth, and the main to secondary sidelobe ratio (MSSR).

5.4 Concluding Remarks

In this work, we start from the study and implementation of dual-seed optical comb sources (Chapter 2), and then incorporate this type of efficient sources into various applications in telecommunications and signal processing. Based on the dual-seed optical comb sources, the target applications investigated here include wavelength multicasting (Chapter 3) and photonic analog-to-digital conversion (Chapter 4). Moreover, it is also promising to apply dual-seed optical comb sources

to microwave photonic signal processing, and one of the examples involves the function of delay-line filters (Chapter 5).

The first contribution of this work is to implement dual-seed optical comb sources capable of simultaneously producing multiple optical frequencies with equidistant separation for wavelength-division-multiplexing (WDM) applications. Two primary challenges including suppression of stimulated Brillouin scattering and the equalization of zero-dispersion wavelength have been overcome by applying a longitudinally varying tension to the optical fibers. In the future, our first work is to further optimize the performance of the optical comb source so that this potential tool can further render a spectrum with broader bandwidth and flatter top.

The second contribution of this work is to demonstrate a wavelength multicasting scheme which possesses not only a feature of modulation format transparency but also a potential for on-chip integration. Based on four-wave mixing with a dual-seed optical comb source in a highly-nonlinear fiber or a silicon waveguide, we experimentally demonstrate 23-way or 14-way wavelength multicasting of 10-Gb/s on-off keying (OOK) data for both media as well as 26-way or 15-way wavelength multicasting of 10-Gb/s differential phase-shift keying (DPSK) data for the two nonlinear media. The dual-seed optical comb source provides multiple spectrally equidistant pump waves leading to a multitude of FWM products after mixing with the signal. In the OOK demonstration, we achieve error-free operation with power penalties less than 4.5 dB for the HNLF and 6.2 dB for the silicon waveguide, respectively. In the DPSK demonstration, we obtain error-free reception with power penalties less than 5.7 dB for the HNLF and 4.2 dB for the

silicon waveguide, respectively. Furthermore, our multicasting scheme also provides a promising approach to on-chip applications which is desirable for future high-speed optical signal processing and WDM communication systems.

The third contribution of this work is to realize a photonic analog-to-digital conversion (ADC) scheme. By utilizing a dual-seed optical comb source and an asymmetric Mach-Zehnder interferometer (MZI), we propose and experimentally validate a photonic analog-to-digital conversion scheme that realizes quantization of a differential radio-frequency analog signal. In the proposed scheme, 4 comb lines carrying various phase harmonics by parametric process are isolated, creating corresponding period-folding transfer functions with respect to the differential phase at the output of the MZI to implement the encoding and quantization. As a proof-of-concept experiment, a quantization level of 8 is obtained for both a simple and a sophisticated signal, respectively. Future work in photonic analog-to-digital conversion involves increase of the number of quantization levels and enhancement of the ability to process sophisticated signals.

Lastly, the fundamentals of photonic microwave delay-line filters have been investigated, and we realize the dual-seed optical comb sources have potential for greatly simplifying the filter design and implementation. In the future, dual-seed optical comb sources will continue to find a wide variety of applications in telecommunications and signal processing.

Bibliography

[1] R. S. Quimby, *Photonics and Lasers: An Introduction*, first edition, Wiley, 2006.

[2] T. Udem, R. Holzwarth, and T. W. Hänsch, "Optical frequency metrology," *Nature* 416(6877), 233–237 (2002).

[3] R. Holzwarth, T. Udem, T. W. Hänsch, J. C. Knight, W. J. Wadsworth, and P. S. Russell, "Optical frequency synthesizer for precision spectroscopy," *Phys. Rev. Lett.* 85(11), 2264–2267 (2000).

[4] T. Steinmetz, T. Wilken, C. Araujo-Hauck, R. Holzwarth, T. W. Hänsch, L. Pasquini, A. Manescau, S. D'Odorico, M. T. Murphy, T. Kentischer, W. Schmidt, and T. Udem, "Laser frequency combs for astronomical observations," *Science* 321(5894), 1335–1337 (2008).

[5] S. T. Cundiff and A. M. Weiner, "Optical arbitrary waveform generation," *Nat. Photonics* 4(11), 760–766 (2010).

[6] D. J. Jones, S. A. Diddams, J. K. Ranka, A. Stentz, R. S. Windeler, J. L. Hall, and S. T. Cundiff, "Carrier-envelope phase control of femtosecond mode-locked lasers and direct optical frequency synthesis," *Science* 288(5466), 635–639 (2000).

BIBLIOGRAPHY

[7] S. T. Cundiff and J. Ye, "Colloquium: femtosecond optical frequency combs," *Rev. Mod. Phys.* 75(1), 325–342 (2003).

[8] H. S. Margolis, "Spectroscopic applications of femtosecond optical frequency combs," *Chem. Soc. Rev.* 41(15), 5174–5184 (2012).

[9] H. R. Telle, G. Steinmeyer, A. E. Dunlop, J. Stenger, D. H. Sutter, and U. Keller, "Carrier-envelope offset phase control: A novel concept for absolute optical frequency measurement and ultrashort pulse generation," *Appl. Phys. B* 69(4), 327–332 (1999).

[10] P. A. Franken, A. E. Hill, C. W. Peters, and G. Weinreich, "Generation of Optical Harmonics," *Phys. Rev. Lett.* 7(4), 118–119 (1961).

[11] R. Boyd, *Nonlinear Optics*, third edition, Academic Press, 2008.

[12] B. E. A. Saleh and M. C. Teich, *Fundamentals of Photonics*, second edition, Wiley, 2007.

[13] D. K. Cheng, *Field and Wave Electromagnetics*, second edition, Addison-Wesley, 1989.

[14] François Cardarelli, *Materials Handbook: A Concise Desktop Reference*, second edition, Springer-Verlag London, 2008.

[15] G. P. Agrawal, *Nonlinear Fiber Optics*, fourth edition, fourth edition, Academic Press, 2006.

[16] S. O. Kasap, *Optoelectronics and Photonics: Principles and Practices*, second edition, Pearson, 2012.

[17] Mark Fox, *Optical Properties of Solids*, second edition, Oxford University Press, 2010.

[18] H. Murata, A. Morimoto, T. Kobayashi, and S. Yamamoto, "Optical pulse generation by electrooptic-modulation method and its application to integrated ultrashort pulse generators," *IEEE J. Sel. Top. Quantum Electron.* 6(6), 1325–1331 (2000).

[19] V. Torres-Company and A. M. Weiner, "Optical frequency comb technology for ultra-broadband radio-frequency photonics," *Laser Photonics Rev.* 8(3), 368–393 (2014).

[20] P. Del'Haye, A. Schliesser, O. Arcizet, T. Wilken, R. Holzwarth, and T. J. Kippenberg, "Optical frequency comb generation from a monolithic microresonator," *Nature* 450(7173), 1214–1217 (2007).

[21] T. J. Kippenberg, R. Holzwarth, and S. A. Diddams, "Microresonator-based optical frequency combs," *Science* 332(6029), 555–559 (2011).

[22] J. S. Levy, A. Gondarenko, M. A. Foster, A. C. Turner-Foster, A. L. Gaeta, and M. Lipson, "CMOS-compatible multiple-wavelength oscillator for on-chip optical interconnects," *Nat. Photonics* 4(1), 37–40 (2010).

[23] M. A. Foster, J. S. Levy, O. Kuzucu, K. Saha, M. Lipson, and A. L. Gaeta, "Silicon-based monolithic optical frequency comb source," *Opt. Express* 19(15), 14233–14239 (2011).

[24] P. L. Christiansen, M. P. Sorensen, and A. C. Scott (Eds.), *Nonlinear Science at the Dawn of the 21st Century*, first edition, Springer-Verlag Berlin Heidelberg, 2000.

[25] K. Inoue, "Four-wave mixing in an optical fiber in the zero-dispersion wavelength region," *J. Lightwave Technol.* 10(11), 1553–1561 (1992).

[26] Y. Ozeki, S. Takasaka, J. Hiroishi, R. Sugizaki, T. Yagi, M. Sakano, and S. Namiki, "Terahertz repetition rate optical pulse train generation based on comb-like profiled fiber," *Digest of the LEOS Summer Topical Meetings*, 115–116 (2005).

[27] E. Myslivets, B. P. P. Kuo, N. Alic, and S. Radic, "Generation of wideband frequency combs by continuous-wave seeding of multistage mixers with synthesized dispersion," *Opt. Express* 20(3), 3331–3344 (2012).

[28] J. M. C. Boggio, J. D. Marconi, and H. L. Fragnito, "Experimental and numerical investigation of the SBS-threshold increase in an optical fiber by applying strain distributions," *J. Lightwave Technol.* 23(11), 3808–3814 (2005).

[29] M. Takahashi, M. Tadakuma, and T. Yagi, "Dispersion and Brillouin managed HNLFs by strain control techniques," *J. Lightwave Technol.* 28(1), 59–64 (2010).

[30] E. Myslivets, C. Lundström, J. M. Aparicio, S. Moro, A. O. J. Wiberg, C.-S. Bres, N. Alic, P. A. Andrekson, and S. Radic, "Spatial equalization of zero-dispersion wavelength profiles in nonlinear fibers," *IEEE Photon. Technol. Lett.* 21(24), 1807–1809 (2009).

[31] V. Ataie, E. Myslivets, B. P.-P. Kuo, N. Alic, and S. Radic, "Spectrally equalized frequency comb generation in multistage parametric mixer with nonlinear pulse shaping," *J. Lightwave Technol.* 32(4), 840–846 (2014).

[32] V. R. Supradeepa and A. M. Weiner, "Bandwidth scaling and spectral flatness enhancement of optical frequency combs from phase-modulated continuous-wave lasers using cascaded four-wave mixing," *Opt. Lett.* 37(15), 3066–3068 (2012).

[33] Frank Träger (Ed.), *Springer Handbook of Lasers and Optics*, second edition, Springer New York, 2007.

[34] R. Malli, X. Zhang, and C. Qiao, "Benefits of multicasting in all-optical networks," *Proc. SPIE* 3531, 209–220 (1998).

[35] B. Mukherjee, "WDM optical communication networks: progress and challenges," *IEEE J. Sel. Areas Comm.* 18(10), 1810–1824 (2000).

[36] J. He, S.-H. G. Chan, and D. H. K. Tsang, "Multicasting in WDM networks," *IEEE Communications Surveys & Tutorials* 4(1), 2–20 (2002).

[37] Y. Yang, "A class of interconnection networks for multicasting," *IEEE Trans. Computers* 47(8), 899–906 (1998).

[38] A. E. Willner, O. F. Yilmaz, J. Wang, X. Wu, A. Bogoni, L. Zhang, and S. R. Nuccio, "Optically efficient nonlinear signal processing," *IEEE J. Sel. Top. Quantum Electron.* 17(2), 320–332 (2011).

[39] C.-S. Bres, S. Zlatanovic, A. O. J. Wiberg, J. R. Adleman, C. K. Huynh, E. W. Jacobs, J. M. Kvavle, and S. Radic, "Parametric photonic channelized RF receiver," *IEEE Photon. Technol. Lett.* 23(6), 344–346 (2011).

[40] S. Khaleghi, O. F. Yilmaz, M. R. Chitgarha, M. Tur, N. Ahmed, S. R. Nuccio, I. M. Fazal, X. Wu, M. W. Haney, C. Langrock, M. M. Fejer, and A. E. Willner, "High-speed correlation and equalization using a continuously tunable all-optical tapped delay line," *IEEE Photon. J.* 4(4), 1220–1235 (2012).

[41] X. Wu, A. Bogoni, S. R. Nuccio, O. F. Yilmaz, M. Scaffardi, and A. E. Willner, "High-speed optical WDM-to-TDM conversion using fiber nonlinearities," *IEEE J. Sel. Top. Quantum Electron.* 16(5), 1441–1447 (2010).

[42] W. Astar, J. B. Driscoll, X. Liu, J. I. Dadap, W. M. J. Green, Y. A. Vlasov, G. M. Carter, and R. M. Osgood, "Tunable wavelength conversion by XPM in a silicon nanowire, and the potential for XPM-multicasting," *J. Lightwave Technol.* 28(17), 2499–2511 (2010).

[43] G. Contestabile, N. Calabretta, R. Proietti, and E. Ciaramella, "Double-stage cross-gain modulation in SOAs: An effective technique for WDM multicasting," *IEEE Photon. Technol. Lett.* 18(1), 181–183 (2006).

[44] L. Xu, N. Chi, K. Yvind, L. Christiansen, L. Oxenløwe, J. Mørk, P. Jeppesen, and J. Hanberg, "7x 40 Gb/s base-rate RZ all-optical broadcasting utilizing an electroabsorption modulator," *Opt. Express* 12(3), 416–420 (2004).

[45] K. K. Chow and C. Shu, "All-optical signal regeneration with wavelength multicasting at 6x10 Gb/s using a single electroabsorption modulator," *Opt. Express* 12(13), 3050–3054 (2004).

[46] C. H. Kwok, S. H. Lee, K. K. Chow, C. Shu, C. Lin, and A. Bjarklev, "Polarization-insensitive all-optical wavelength multicasting by self-phase-modulation in a photonic-crystal fiber," in *Proceedings of CLEO 2006*, Long Beach, CA, May 2006, Paper CTuD4.

[47] A. Biberman, B. G. Lee, A. C. Turner-Foster, M. A. Foster, M. Lipson, A. L. Gaeta, and K. Bergman, "Wavelength multicasting in silicon photonic nanowires," *Opt. Express* 18(17), 18047–18055 (2010).

[48] C.-S. Brès, N. Alic, E. Myslivets, and S. Radic, "Scalable multicasting in one-pump parametric amplifier," *J. Lightwave Technol.* 27(3), 356–363 (2009).

[49] M. Pu, H. Hu, H. Ji, M. Galili, L. K. Oxenløwe, P. Jeppesen, J. M. Hvam, and K. Yvind, "One-to-six WDM multicasting of DPSK signals based on dual-pump four-wave mixing in a silicon waveguide," *Opt. Express* 19(24), 24448–24453 (2011).

[50] G. W. Lu, K. S. Abedin, and T. Miyazaki, "DPSK multicast using multiple-pump FWM in Bismuths highly nonlinear fiber with high multicast efficiency," *Opt. Express* 16(26), 21964–21970 (2008).

[51] D. Wang, T.-H. Cheng, Y.-K. Yeo, J. Liu, Z. Xu, Y. Wang, and G. Xiao, "All-optical modulation-transparent wavelength multicasting in a highly nonlinear fiber Sagnac loop mirror," *Opt. Express* 18(10), 10343–10353 (2010).

[52] C.-S. Brès, A. O. J. Wiberg, B. P.-P. Kuo, N. Alic, and S. Radic, "Wavelength multicasting of 320-Gb/s channel in self-seeded parametric amplifier," IEEE *Photon. Technol. Lett.* 21(14), 1002–1004 (2009).

[53] B. P.-P. Kuo, E. Myslivets, N. Alic, and S. Radic, "Wavelength multicasting via frequency comb generation in a bandwidth-enhanced fiber optical parametric mixer," *J. Lightwave Technol.* 29(23), 3515–3522 (2011).

[54] M. A. Foster, A. C. Turner, R. Salem, M. Lipson, and A. L. Gaeta, "Broad-band continuous-wave parametric wavelength conversion in silicon nanowaveguides," *Opt. Express* 15(20), 12949–12958 (2007).

[55] A. C. Turner-Foster, M. A. Foster, R. Salem, A. L. Gaeta, and M. Lipson, "Frequency conversion over two-thirds of an octave in silicon nanowaveguides," *Opt. Express* 18(3), 1904–1908 (2010).

[56] V. R. Almeida, R. R. Panepucci, and M. Lipson, "Nanotaper for compact mode conversion," *Opt. Lett.* 28, 1302-1304 (2003).

[57] A. Gajda, L. Zimmermann, M. Jazayerifar, G. Winzer, H. Tian, R. Elschner, T. Richter, C. Schubert, B. Tillack, K. Petermann, "Highly efficient CW parametric conversion at 1550 nm in SOI waveguides by reverse biased p-i-n junction," *Opt. Express* 20(12), 13100–13107 (2012).

[58] M. J. R. Heck, J. F. Bauters, M. L. Davenport, J. K. Doylend, S. Jain, G. Kurczveil, S. Srinivasan, Y. Tang, and J. E. Bowers, "Hybrid Silicon Photonic Integrated Circuit Technology," *IEEE J. Quantum Electron.* 19(4), 6100117 (2013).

[59] D. G. Manolakis and V. K. Ingle, *Applied Digital Signal Processing: Theory and Practice*, first edition, Cambridge University Press, 2011.

[60] P. Ghelfi, F. Laghezza, F. Scotti, G. Serafino, A. Capria, S. Pinna, D. Onori, C. Porzi, M. Scaffardi, A. Malacarne, V. Vercesi, E. Lazzeri, F. Berizzi, and A. Bogoni, "A fully photonics-based coherent radar system," *Nature* 507(7492), 341–345 (2014).

[61] M. Yip and A. P. Chandrakasan, "A Resolution-Reconfigurable 5-to-10-Bit 0.4-to-1 V Power Scalable SAR ADC for Sensor Applications," *IEEE Journal of Solid-State Circuits* 48(6), 1453–1464 (2013).

[62] P. Cruz, N. B. Carvalho and K. A. Remley, "Designing and Testing Software-Defined Radios," *IEEE Microwave Magazine* 11(4), 83–94 (2010).

[63] R. H. Walden, "Analog-to-digital converter survey and analysis," *IEEE J. Sel. Areas Comm.* 17(4), 539–550 (1999).

[64] G. C. Valley, "Photonic analog-to-digital converters," *Opt. Express* 15(5), 1955–1982 (2007).

[65] F. A. Coppinger, A. S. Bhushan, and B. Jalali, "Photonic time stretch and its application to analog-to-digital conversion," *IEEE Trans. Microw. Theory Tech.* 47(7), 1309–1314 (1999).

[66] Y. Han and B. Jalali, "Photonic time-stretched analog-to-digital converter: Fundamental concepts and practical considerations," *J. Lightwave Technol.* 21(12), 3085–3103 (2003).

[67] T. R. Clark, J. U. Kang, and R. D. Esman, "Performance of a Time- and Wavelength-Interleaved Photonic Sampler for Analog–Digital Conversion," *IEEE Photon. Technol. Lett.* 11(9), 1168–1170 (1999).

[68] M. P. Fok, K. L. Lee, and C. Shu, "4×2.5 GHz repetitive photonic sampler for high-speed analog-to-digital signal conversion," *IEEE Photon. Technol. Lett.* 16(3), 876–878 (2004).

[69] H. F. Taylor, "An electro-optic analog-to-digital converter," *Proc. IEEE* 63(10), 1524–1525 (1975).

[70] B. Jalali and Y. M. Xie, "Optical folding-flash analog-to-digital converter with analog encoding," *Opt. Lett.* 20(18), 1901–1903 (1995).

[71] M. Currie, T. R. Clark, and P. J. Matthews, "Photonic analog-to-digital conversion by distributed phase modulation," *IEEE Photon. Technol. Lett.* 12(12), 1689–1691 (2000).

[72] J. Stigwall and S. Galt, "Interferometric analog-to-digital conversion scheme," *IEEE Photon. Technol. Lett.* 17(2), 468–470 (2005).

[73] J. Stigwall and S. Galt, "Demonstration and analysis of a 40-gigasample/s interferometric analog-to-digital converter," *J. Lightwave Technol.* 24(3), 1247–1256 (2006).

[74] W. Li, H. Zhang, Q. Wu, Z. Zhang, and M. Yao, "All-optical analog-to-digital conversion based on polarization-differential interference and phase modulation," *IEEE Photon. Technol. Lett.* 19(8), 625–627 (2007).

[75] Q. Wu, H. Zhang, M. Yao, W. Zhou, "All-optical analog-to-digital conversion using inherent multiwavelength phase shift in $LiNbO_3$ phase modulator," *IEEE Photon. Technol. Lett.* 20(12), 1036–1038 (2008).

[76] C. H. Sarantos and N. Dagli, "A photonic analog-to-digital converter based on an unbalanced Mach-Zehnder quantizer," *Opt. Express* 18(14), 14598–14603 (2010).

[77] H. Chi, Z. Li, X. Zhang, S. Zheng, X. Jin, and J. P. Yao, "Proposal for photonic quantization with differential encoding using a phase modulator and delay-line interferometers," *Opt. Lett.* 36(9), 1629–1631 (2011).

[78] Y. Chen, H. Chi, S. Zheng, X. Zhang and X. Jin, "Differentially Encoded Photonic Analog-to-Digital Conversion Based on Phase Modulation and Interferometric Demodulation," *IEEE Photon. Technol. Lett.* 23(24), 1890–1892 (2011).

[79] J. Kakande, R. Slavik, F. Parmigiani, A. Bogris, D. Syvridis, L. Grüner-Nielsen, R.P. Petropoulos, and D. J. Richardson, "Multilevel quantization of optical phase in a novel coherent parametric mixer architecture," *Nat. Photonics* 5(12), 748–752 (2011).

[80] V. J. Urick, F. Bucholtz, P. S. Devgan, J. D. McKinney, and K. J. Williams, "Phase Modulation With Interferometric Detection as an Alternative to Intensity Modulation With Direct Detection for Analog-Photonic Links," *IEEE Trans. Microw. Theory Tech.* 55(9), 1978–1985 (2007).

[81] H. Chi and J. Yao, "A photonic analog-to-digital conversion scheme using Mach-Zehnder modulators with identical half-wave voltages," *Opt. Express* 16(2), 567–572 (2008).

[82] J. Yao, "Microwave photonics," *J. Lightwave Technol.* 27(3), 314–335 (2009).

[83] B. Vidal, V. Polo, J. L. Corral, and J. Marti, "Efficient architecture for WDM photonic microwave filters," *IEEE Photon. Technol. Lett.* 16(1), 257–259 (2004).

[84] J. Sancho, J. Bourderionnet, J. Lloret, S. Combrié, I. Gasulla, S. Xavier, S. Sales, P. Colman, G. Lehoucq, D. Dolfi, J. Capmany, and A. De Rossi, "Integrable microwave filter based on a photonic crystal delay line," *Nat. Commun.* 3(article 1075), 1–9 (2012).

[85] J. Capmany, J. Mora, I. Gasulla, J. Sancho, J. Lloret, and S. Sales, "Microwave photonic signal processing," *J. Lightwave Technol.* 31(4), 571–586 (2013).

[86] A. Loayssa, J. Capmany, M. Sagues, and J. Mora, "Demonstration of incoherent microwave photonic filters with all-optical complex coefficients," *IEEE Photonics Technol. Lett.* 18(16), 1744–1746 (2006).

[87] M. Sagues, A. Loayssa, and J. Capmany, "Multitap complex-coefficient incoherent microwave photonic filters based on stimulated Brillouin scattering," *IEEE Photon. Technol. Lett.* 19(16), 1194–1196 (2007).

[88] J. Lloret, J. Sancho, M. Pu, I. Gasulla, K. Yvind, S. Sales, and J. Capmany, "Tunable complex-valued multi-tap microwave photonic filter based on single silicon-on-insulator microring resonator," *Opt. Express* 19(13), 12402–12407 (2011).

[89] S. Khaleghi, M. R. Chitgarha, O. F. Yilmaz, M. Tur, M. W. Haney, C. Langrock, M. M. Fejer, and A. E. Willner, "Experimental performance of a fully tunable complex-coefficient optical FIR filter using wavelength conversion and chromatic dispersion," *Opt. Lett.* 37(16), 3420-3422 (2012).

[90] Y. Zhang and S. Pan, "Tunable multitap microwave photonic filter with all complex coefficients," *Opt. Lett.* 38(5), 802–804 (2013).

Vita

Hong-Fu Ting was born in 1982 in Taipei, Taiwan (R.O.C.). He received his B.S. degree in Physics from National Chung Hsing University, Taiwan (R.O.C.) in 2005. In 2009, he came to the United States and pursued a master's degree in Electrical and Computer Engineering from Johns Hopkins University where he joined Dr. Mark A. Foster's research group (Ultrafast & Nonlinear Photonics Group) in 2011 to further pursue a Ph.D. degree. He received his M.S.E. in May, 2012, and successfully defended his Ph.D. dissertation in January, 2017. His research interest includes applications of nonlinear fiber optics in optical communications and optical signal processing.